Evolution of Secondary Organic Aerosol Composition, Volatility, and Absorption During Oxidation of Phenolic Compounds Under Conditions Relevant to Biomass Burning

Carley Fredrickson

A thesis

submitted in partial fulfillment of the

requirements for the degree of

Master of Science

University of Washington

2021

Committee:

Joel Thornton

Becky Alexander

Lyatt Jaeglé

Program Authorized to Offer Degree:

Atmospheric Sciences

University of Washington

Abstract

Evolution of Secondary Organic Aerosol Composition, Volatility, and Absorption During Oxidation of Phenolic Compounds Under Conditions Relevant to Biomass Burning

Carley Fredrickson

Chair of the Supervisory Committee:
Joel Thornton
Department of Atmospheric Sciences

Phenolic compounds emitted from wildfires and biomass burning (BB) are highly reactive and yield secondary organic aerosol (SOA) and brown carbon (BrC) upon oxidation initiated by the hydroxyl radical (OH) and nitrate radical (NO_3). In high nitrogen dioxide (NO_2) environments, such as BB plumes, phenolic oxidation is expected to form nitroaromatics in high yield which can explain in part the BrC content of associated SOA. We conducted a set of experiments as part of the Monoterpene and Oxygenated aromatics Oxidation at Night and under LIGHTs (MOONLIGHT) campaign to evaluate the chemical and physical drivers of phenolic compound evolution in high nitrogen oxide ($NO_x = NO + NO_2$) wildfire plumes, specifically investigating the composition, volatility, and absorption of the SOA components formed under OH and NO_3 oxidation, with catechol as the focus of this thesis. Oxidation products in both the gas and particle phases were measured using an I^- adduct high-resolution time-of-flight chemical ionization mass spectrometer (HR-ToF I^- CIMS) coupled with the Filter Inlet for Gases and Aerosols (FIGAERO). Oxidation of catechol produced BrC, defined by light absorption at

405 nm, at the highest yields out of all the phenolics studied. Particle-phase nitrocatechol ($C_6H_5NO_4$) was found to account for 28% and 79% of organic aerosol (OA) mass formed from OH-initiated or NO_3-initiated oxidation, respectively, and was strongly associated with BrC. Effective molar yields, i.e., including chemical and physical losses, of nitrocatechol were measured to range from 0.65 to 1 for NO_3-initiated oxidation, and 0.03 for OH oxidation conditions. Maximum SOA mass yields from catechol oxidation were strongly tied to formation of nitrocatechol, ranging from 0.38 to 1.63 for the different experiments, lower than previously reported values. Higher SOA mass yields from catechol oxidation were found for NO_3 rather than OH oxidation. The effective volatility of the SOA measured with the FIGAERO thermograms decreased significantly with subsequent aging after formation. Gas-particle partitioning measurements imply the saturation vapor concentration of nitrocatechol to be roughly 5 $\mu g\ m^{-3}$, while the FIGAERO thermogram model estimate is lower but in the same order of magnitude, implying that wildfire gas-particle partitioning of nitroaromatics is likely dynamic. Group contribution method estimates of nitrocatechol saturation concentration range across 8 orders of magnitude with 3 $\mu g\ m^{-3}$ from the Nannoolal method paired with the Joback and Reid boiling point method being closest to our observational estimates. In extended photochemical aging experiments, BrC formed from catechol oxidation had a photochemical lifetime of ~12 hours, while that of particulate nitrocatechol ranged from 7 hours if formed by NO_3 oxidation to 18 hours if formed by OH oxidation. Implications for atmospheric evolution of BrC in wildfire and mechanisms of particulate nitroaromatic losses are discussed.

TABLE OF CONTENTS

LIST OF FIGURES iii

LIST OF TABLES v

Chapter 1. INTRODUCTION 7

Chapter 2. METHODS 14

2.1. MOONLIGHT Chamber Experiment Overview 14

2.2. Instrumentation 17

2.3. SOA Yield and Volatility 19

Chapter 3. RESULTS AND DISCUSSION 26

3.1. SOA Yields 26

3.2. Gas and Particle Composition of Catechol Oxidation 29

3.3. Observed Thermogram Properties and Evolution 33

3.4. Constraints on the nitrocatechol C^* 36

3.5. Evolution of particulate absorption 42

Chapter 4. CONCLUSIONS 45

REFERENCES 49

Appendix A. TOTAL EXPERIMENTAL CHAMBER CONDITIONS 58

Appendix B. EVERY EXPERIMENT NITROCATECHOL THERMOGRAMS 64

Appendix C. ADDITIONAL CATECHOL EXPERIMENT ABSORPTION DECAY 66

Appendix D. FIGAERO-CIMS OA AND AMS OA TRENDS 67

Appendix E. NITROCATECHOL DIVIDED THERMOGRAM CONTRIBUTIONS 70

LIST OF FIGURES

Figure 1. Time series of the notable increasing gas-phase compounds in two experiments. Left: The catechol + OH/NO_x experiment. Right: The catechol + O_3 + NO_3 extended experiment. Grey shading indicates when the lights were off. Organics other than nitrocatechol ($C_6H_5NO_4$) and catechol ($C_6H_6O_2$) are colored by carbon number, while nitrogen-containing compounds are all colored maroon. 30

Figure 2. Time series of the notable particle-phase compounds in two experiments. Top: The catechol + OH/NO_x experiment. Bottom: The catechol + O_3 + NO_3 extended experiment. Nitrocatechol ($C_6H_5NO_4$) is plotted on the blue left y-axis for both plots and all other compounds are plotted on the black right y-axis. Grey shading indicates when the lights were off. Organics are colored by carbon number, while nitrogen-containing compounds are all colored maroon, excluding nitrocatechol ($C_6H_5NO_4$). 32

Figure 3. The OA composition for the two experiments at peak OA signal. Left: Catechol + OH/NO_x experiment. Right: Catechol + O_3 + NO_3 extended experiment. 33

Figure 4. Nitrocatechol thermograms colored by increasing experiment time (increasing desorption number) from blue to yellow since the start of the 06/14 catechol + O_3 + NO_3 extended experiment. Left: Thermogram of absolute signal. Right: Thermogram of normalized signal. Filter blank thermograms are not included in this plot. 35

Figure 5. Time series of the integrated normalized nitrocatechol thermograms from Figure 4 with the integrations separated at a temperature of 110 °C and normalized by AMS SO_4 to normalize by chamber wall losses for the 06/14 catechol + O_3 + NO_3 extended experiment. 36

Figure 6. Calculated F_p versus observed F_p for all catechol experiments where open squares symbolize the catechol + OH/NO_x experiment and closed circles symbolize the catechol + O_3 + NO_3 experiments. Blue, red, and yellow markers denote fixed C^* of 5, 10, and 50 $\mu g\ m^{-3}$, respectively. The markers grow as experiment time increases. The 1:1 line is encoded as a dashed line and ±30% uncertainty ranges reflecting a conservative estimate from calibration and instrument precision uncertainties is encoded as solid gray lines........ 37

Figure 7. Comparing different C^* estimations. Each color of the dots represents a different group-contribution method, with MCM-provided SMILES strings in the darker color and the PubChem-provided SMILES strings in the lighter color. Each shape denotes a different boiling point method used. SIMPOL.1 did not use a SMILES string. Volatility classes are shaded in the background and colored as in Chuang and Donahue (2016). 40

Figure 8. Fit of the catechol + O_3 + NO_3 nitrocatechol's ($C_6H_5NO_4$) first thermogram. Observational data is encoded as a black line while the model fit is encoded as a green line. 41

Figure 9. The 06/03 catechol + OH/NO_x experiment. Left: Time series of the absorption as measured by the PAS at 405 nm and mass concentrations of AMS OA, and particle-phase nitrocatechol. Right: The same measurements normalized by AMS SO_4. Some data have been multiplied by factors to compare the shapes of the different curves. Exponential decay fits of each variable are plotted as dashed lines. Lifetimes, τ, of these fits are reported in the figure text. 43

Figure 10. Similar to **Figure 9**, but for the 06/05 catechol + O_3 + NO_3 extended experiment. Left: Absolute measurements. Right: Measurements normalized to AMS SO_4. Some data have been multiplied by factors to compare the shapes of the different curves. Exponential decay fits of each variable are plotted as dashed lines. Lifetimes, τ, of these fits are reported in the figure text.......... 44

LIST OF TABLES

Table 1. Chamber conditions for all catechol oxidation experiments. 16

Table 2. SOA yields for all catechol oxidation experiments... 28

Table 3. Molar yields of nitrocatechol for all catechol oxidation experiments........................... 28

ACKNOWLEDGEMENTS

I would like to thank my advisor, Joel Thornton, for his mentorship, insights, and support. I would also like to thank my thesis committee members – Joel Thornton, Becky Alexander, and Lyatt Jaeglé – for their feedback and encouragement throughout this process. Lastly, I would like to thank the collaborators on this project – Brett Palm, Ben Lee, Xuan Zhang, Lauren Garofalo, Matson Pothier, Delphine Farmer, Zachary Decker, Steven Brown, Shane Murphy, Yingjie Shen, Amy Sullivan, and Siegfried Schobesberger for their respective expertise and for sharing their data. I want to recognize the Thornton group members past and present; Ben Lee, Brett Palm, Qiaoyun Peng, Jessica Haskins, and Phil Rund; as well as my cohort; Yuk Chun Chan, Tyler Cox, Andrew DeLaFrance, Lily Hahn, Daniel Lloveras, Jacqueline Nugent, Phil Rund, Clayton Sasaki, Greta Shum, Adam Sokol, Lindsey Taylor, Sami Turbeville, Mingcheng Wang, and Claire Zarakas; and the Atmospheric Sciences staff for providing motivation and helping me move forward. It has been a particularly difficult time this past year due to the COVID-19 pandemic, but with the added support from my family, friends, and Myles I was able to complete this thesis.

This project was entirely funded by the National Science Foundation through grant number NSF AGS 1652688. I would also like to acknowledge support from the National Oceanic and Atmospheric Administration for the FIREX-AQ campaign with the NOAA OAR Climate Program Office Award Number NA17OAR4310012 as well as the National Aeronautics and Space Administration with the Future Investigators in NASA Earth and Space Science and Technology (FINESST) grant no. 80NSSC20K1612.

Chapter 1. INTRODUCTION

In the western United States, the number of large wildfires, the length of the wildfire season, and the area burned by wildfires have been increasing and they are predicted to continue to rise (Barbero et al. 2015; Dennison et al. 2014; Jolly et al. 2015; Short 2015). The gaseous and particulate emissions from these fires, also denoted as biomass burning, adversely affect human health, impair visibility, and impact our climate due to particle-light interactions, also known as its optical properties (Bond et al. 2013; Karanasiou et al. 2021; Laskin, Laskin, and Nizkorodov 2015). The impact of biomass burning on the global and annual mean radiative forcing, a measure of a factor's influence on Earth's radiative budget, remains uncertain, with the latest IPCC assessment report associating 0.0 W m^{-2} radiative forcing from direct and semi-direct biomass burning aerosol-radiation interactions with uncertainties ranging from -0.20 to 0.20 W m^{-2} (Myhre et al. 2013). The uncertainties in the biomass burning radiative forcing estimate come from model uncertainty and the likelihood that biomass burning emissions are underestimated (Boucher et al. 2013).

Biomass burning emits carbon dioxide, carbon monoxide, methane, black carbon, primary organic aerosol (POA), reactive nitrogen like nitric oxides (NO_x), volatile organic compounds (VOCs), etc., the latter two being important for the production of ozone, secondary organic aerosol (SOA), and brown carbon (BrC), a component of organic aerosol that strongly absorbs in the ultraviolet and visible wavelengths (Akagi et al. 2011; M. O. Andreae and Merlet 2001; Meinrat O. Andreae 2019; Buysse et al. 2019; Jaffe and Wigder 2012; Koss et al. 2018; Laskin, Laskin, and Nizkorodov 2015; Palm et al. 2020). It is not clear how much SOA is produced from biomass burning due to concurrent OA loss and formation processes within the smoke. SOA can be formed via multiple pathways. As it has been traditionally known, VOCs can undergo gas-phase oxidation reactions, effectively increasing the number of oxygens bonded to the parent VOC, resulting in a less volatile compound that subsequently condenses either on already formed particles through heterogeneous nucleation, or by forming new particles via homogeneous nucleation. SOA can also be formed via aqueous oxidation. This process is characterized by water-soluble gas-phase oxidation products of VOCs that partition onto aqueous particles, such as fog or cloud droplets. Those water-soluble products then further react to yield compounds that have a higher tendency to stay in the particle phase. When the water on aqueous particles evaporates, these compounds remain and are collectively known as aqueous SOA. Finally, SOA can be formed from the gas-phase oxidation of semivolatile components driven off POA under conditions of dilution, recondensing in the particle phase. This last pathway makes biomass burning SOA (BBSOA) formation rates difficult to ascertain since current bulk measurements of organic aerosol (OA) cannot quantitatively determine how much biomass burning POA (BBPOA) has evaporated and how much BBSOA has been formed. In field measurements, Garofalo et al. (2019) reported that the normalized excess mixing ratios (NEMRs) for biomass burning OA (BBOA) mass stayed level with increasing smoke plume age in the wildfires sampled during the Western wildfire Experiment for Cloud chemistry, Aerosol absorption and Nitrogen (WE-CAN), resulting from competition between dilution-driven evaporation and oxidation-driven condensation. In a smoke plume dilution analysis, Palm et al. (2020) estimated that within the same WE-CAN wildfires up to one third of BBPOA evaporates, reacts and then subsequently forms BBSOA with near unit yield in cases of high smoke plume dilution.

One class of VOCs emitted from biomass burning are phenolic compounds, classified by the presence of a benzene ring with one hydroxy substituent. Under high temperatures, lignin found in wood tissues and bark undergoes pyrolysis, breaking into the smaller components known as phenolics. Research on phenolic compounds have gained popularity in the atmospheric chemistry community as they are suspected SOA precursors. Oxidation of these compounds by the hydroxyl radical (OH) has been extensively studied and this reaction produces SOA with yields as high as 145% (Finewax, de Gouw, and Ziemann 2018; Lauraguais et al. 2014; Nakao et al. 2011; Pereira et al. 2015; Yee et al. 2013). Few of these studies also incorporated NO_x, which produced substantial BrC due to the presence of light-absorbing nitroaromatic compounds (Finewax, de Gouw, and Ziemann 2018; Lin et al. 2015; Romonosky et al. 2015).

While atmospheric oxidation is driven in large part by solar radiation-induced radicals like OH, dark chemistry with the nitrate radical (NO_3) can be important for NO_3-reactive compounds. Millet et al. (2016) discovered that in a city downwind of an isoprene-emitting forest, nighttime chemistry with NO_3 controlled isoprene's fate and the probability of a high-O_3 occurrence in the city the following day. Research on the oxidation of phenolic compounds with NO_3 has been understudied. It has been found that nitroaromatic compounds primarily compose the SOA from phenolic reaction with NO_3, show significant BrC character, and have SOA yields that can be as high as 161% (Bolzacchini et al. 2001; Finewax, de Gouw, and Ziemann 2018; Mayorga, Zhao, and Zhang 2021). These airborne nitroaromatic compounds are toxic, mutagenic, and carcinogenic (Kovacic and Somanathan 2014; Kroflič, Grilc, and Grgić 2015; Leuenberger et al. 1988; Traversi et al. 2009). Nitroaromatic compounds strongly absorb UV-Vis radiation, contributing to BrC. Mohr et al. (2013) showed that just a few nitrated phenolic compounds measured in authentic biomass burning aerosol can explain at least 5–10% of biomass burning aerosol light absorption at 370 nm. While BrC is being incorporated into global climate models, the yields, lifetimes, and optical properties of SOA and BrC from wildfire smoke chemistry have not been extensively quantified under nighttime conditions. Moreover, it remains unclear whether photochemistry or nocturnal chemistry of phenolic compounds is a more efficient source of BrC and whether the associated BrC is long-lived under typical atmospheric conditions.

The evolution of BBOA, in terms of POA loss, SOA formation, and optical properties such as BrC "bleaching" is likely complex and yet to be fully understood. Hennigan et al. (2011) found that unreacted POA contributed to 17% of the FLAME III campaign-average OA mass after 3.5 hours of exposure to atmospherically-relevant OH concentrations, while Forrister et al. (2015) reported that BrC absorption decayed in plumes with a half-life of 9 to 15 hours, demonstrating conflicting aerosol processing rates. Saleh et al. (2014) concluded that since the absorptivity of BBOA can be derived from the ratio of black carbon to OA, aerosol absorptivity depends largely on burn conditions, not fuel type, yet Lack et al. (2013) stated that mass absorption efficiency of particulate organic matter at 404 nm has a robust relationship with the ratio of f60 (levoglucosan) to f44 (oxidized organics), suggesting that the strength of BrC absorption can be predicted by emissions of levoglucosan-related organic matter.

Knowing the extent of a compound's partitioning into either the gas phase or particle phase is critical to determine its evolution, as gas-phase chemical processing rates are different from particle-phase chemical processing. One of the primary properties that determines how a chemical compound will partition is volatility. Volatility, defined as a propensity to evaporate from the condensed phase, can be represented by its saturation vapor pressure referenced to the pure substance, shown in equation 1,

$$k_{e,i} = \frac{k_{c,i}}{C_{OA}} \left(\frac{M_i 10^6 \zeta'_i p^o_{L,i}}{760\ R\ T} \right) \tag{1}$$

where $k_{e,i}$ is the rate coefficient for evaporation of compound i, $k_{c,i}$ is the rate coefficient for condensation of compound i, C_{OA} is the OA mass concentration, M_i is the molecular weight of compound i, $\zeta_i^{'}$ is the molality-based activity coefficient for compound i, $p_{L,i}^{o}$ is the saturation vapor pressure for compound i at temperature T as a pure liquid, and R is the gas constant. Notice that as the saturation vapor pressure increases, the rate coefficient of evaporation of compound i increases. For considerations of OA, typically reported in mass concentration units, we use the saturation vapor concentration, which is directly related to the saturation vapor pressure through a unit conversion. The saturation vapor concentration, C^o, is an intrinsic property of a molecule that depends upon its structure since the structure dictates the intermolecular interactions, such as binding or solvation, that the molecule experiences on surfaces or with components of a solution, and also depends on its size (molecular mass). A molecule can thus have a different saturation vapor concentration above a mixture compared to that above the pure substance due to different types of interactions. These “non-idealities” are usually considered with an activity coefficient used to scale the saturation vapor concentration referenced to the pure substance, $C^* = \zeta^{'} C^o$, where C^* represents the effective volatility. Given the complexity of OA, which can be a mixture of hundreds or thousands of different components, non-idealities are typically ignored and/or order-of-magnitude C^* bins are utilized to predict the evolution of the mixture’s volatility distribution. Several group-contribution methods have been developed to parameterize C^* for atmospherically-relevant organic compounds in terms of molecular size and structure, namely the number and type of functional groups (Compernolle, Ceulemans, and Müller 2011; Myrdal and Yalkowsky 1997; Nannoolal, Rarey, and Ramjugernath 2008; Pankow and Asher 2008). However, only limited tests of these parameterizations have been conducted using actual organic aerosol systems.

Volatility is fundamental to gas-particle partitioning theory. Gas-particle partitioning theory describes what fraction of a compound i can be found in the particle phase. We can relate this fraction to such quantities like the equilibrium partitioning coefficient, $K_{p,i}$, the total mass concentration of the absorbing particle phase, C_{OA}, and the saturation vapor concentration, C_i^*:

$$\frac{C_i^p}{C_i^g} = K_{p,i}C_{OA} = \frac{C_{OA}}{C_i^*} \tag{2}$$

where C_i^p is the mass concentration of compound i in the particle phase and C_i^g is the mass concentration of compound i in the gas phase. With a little more rearrangement, we can quantify the fraction in the particle phase of compound i.

$$F_i = \frac{C_i^p}{C_i^p+C_i^g} = \frac{C_{OA}K_{p,i}}{1+C_{OA}K_{p,i}} = \frac{1}{1+\frac{C_i^*}{C_{OA}}} \tag{3}$$

Each compound's fraction in the particle phase can then be multiplied by the mass-based stoichiometric yield of each compound and then be summed over all compounds to predict the partitioning of bulk aerosol and the SOA yield. This theory does have its limitations. First, SOA formation can involve a plethora of gas-phase and particle-phase compounds, yet at any point in time, we likely know a limited amount. Of the few that we do know, yields of these compounds are often on the order of a few percent, making them hard to parameterize in models and susceptible to experimental error. Second, C_{OA} is not solely the total organic aerosol, but total absorbing aerosol, thus assumptions are made about how much mass we can attribute to the condensing phase. Third, C_i^* is a temperature-dependent property relying on accurate measurements of individual compounds' enthalpies of vaporization, but these measurements are scarce. Fourth, vapor pressures are hard to determine, the role of relative humidity on this partitioning theory is unknown, and the ambient atmosphere is more complex than the synthetically created atmosphere in the laboratory. Fifth, there is an uncertainty due to experimental artifacts such as aerosol loss to chamber surfaces. Sixth, products that are important for SOA formation can continue to react into different products. Lastly, gas-phase and particle-phase reactions shift the equilibria of the system, meaning that the fraction in the particle phase is also a function of the rate of change of the mass concentrations in the gas and particle phase (Hallquist et al. 2009).

To properly understand the fate of SOA in wildfire smoke plumes, it is necessary to quantify the volatilities, yields, and fraction in the particle phase for those phenolics that undergo rapid oxidation. The scope of this paper focuses on the properties of an important precursor of SOA and BrC, catechol ($C_6H_6O_2$). During the WE-CAN, an I^- CIMS reported rapid loss of a sizable amount of catechol with plume aging throughout the campaign. With excessive amounts of NO_x and limited photochemistry in thick plumes, catechol is thought to be reacting with the nitrate radical (NO_3) and the hydroxyl radical (OH). In earlier laboratory experiments, catechol was found to predominantly produce 4-nitrocatechol ($C_6H_5NO_4$) in SOA via abstraction of a phenolic H by either radical followed by a second reaction with NO_2, but ignored how the composition changes with aging (Finewax, de Gouw, and Ziemann 2018). In a series of experiments conducted in the National Center for Atmospheric Research (NCAR) environmental chamber, we quantified gas-phase and particle-phase composition, absorption, volatility, and evolution of SOA formed from catechol daytime and nighttime oxidation under conditions relevant to wildfire smoke and conducive to aging.

Chapter 2. METHODS

2.1. MOONLIGHT Chamber Experiment Overview

The Monoterpene and Oxygenated Aromatics Oxidation at Night and Under Lights (MOONLIGHT) community project was a multi-institution effort to investigate the daytime (OH-initiated) and nighttime (NO_3-initiated) oxidation of a specific subset of VOCs emitted by biomass burning and was conducted from May to June 2019 to complement the findings from WE-CAN. These VOCs consisted of phenolics and furans: phenol, catechol, cresol, guaiacol, and furfural. In this paper, we will be discussing results from the catechol experiments. Experiments involving limonene and α-pinene were conducted as well. Experiments were conducted within NCAR's 10 m^3 FEP Teflon chamber housed in a cubic enclosure with UV-reflective surfaces surrounded by 128 blacklight tubes (32W, Type F32T8/BL). In this chamber j_{NO2} was measured to be 1.24×10^{-3} s^{-1} at 100% light intensity. The chamber temperature was kept at a constant 295 K when the blacklights were off and increased to ~305 K when the blacklights were operated at full capacity. All reactants and products were passively mixed within the chamber. For all catechol experiments, the relative humidity of the chamber was kept below 10% and ammonium sulfate dry seeds with a monomodal size distribution and maximum mass at a vacuum aerodynamic diameter of 350 nm were injected to prevent absorption onto the chamber walls. At the end of each experiment, the chamber was cleaned at the very least overnight by flowing only ultra-high-purity (UHP) nitrogen through it. Peak SOA measured by an aerosol mass spectrometer (AMS) ranged from 3 to 30 μg m^{-3} in these catechol experiments, though in some cases described below, SOA was produced on particles larger than the AMS can sample and thus these are lower limits to the total SOA produced. Individual details about each experiment can be found in **Table 1** and the time series of select gas-phase and particle-phase components during each experiment can be found in Appendix A.

Date (mm/dd/yyyy)	Experiment	Oxidant Type	Duration (mins)	Reacted Catechol (ppb)	Seed Concentration Pre-Oxidant (µg sm^{-3})	AMS Maximum OA Produced (µg sm^{-3})
06/03/2019	Daytime	OH	399	18	62	26
06/04/2019	Nighttime with photobleaching	NO_3	230	5.8	101	28
06/05/2019	Nighttime with extended photobleaching	NO_3	1120	19	115	41
06/14/2019	Nighttime with extended photobleaching without O_3	NO_3	1103	18	94	38
06/22/2019	Nighttime with extended aging (no lights)	NO_3	1205	7.7	160	39

Table 1. Chamber conditions for all catechol oxidation experiments.

2.2. Instrumentation

Measurements of total OA, total sulfate aerosol, and total ammonium aerosol were performed by the Colorado State University's Aerosol Mass Spectrometer (HR-AMS; Aerodyne, Inc) and Aerosol Chemical Speciation Monitor (ACSM). A more thorough description of their instrumentation can be found in DeCarlo et al. (2006) and Ng et al. (2011). HR-AMS output (μg m^{-3}) was converted to μg sm^{-3} by adjusting to sea level pressure while temperature was not adjusted for. Measurements of ozone were made by a UV-absorption ozone monitor (Model 49i-PIS, ThermoScientific) while NO and NO_2 were measured with a chemical luminescence NO_x and chemical luminescence NO detector (Model CLD 88Y, EcoPhysics). Additional measurements of NO, NO_2, and O_3 were also performed by the National Oceanic and Atmospheric Administration's nitrogen oxide cavity ring down spectrometer (Brown et al. 2017). A multi-channel photoacoustic spectrometer (PAS) provided by the University of Wyoming, as described in Foster et al. (2019), was used to measure dry aerosol absorption at 405 and 660 nm. Colorado State University's Particle-into-Liquid-Sampler Liquid-Waveguide-Capillary-Cell Total-Organic-Carbon (PILS-LWCC-TOC) instrument measured the water-soluble BrC absorption at 405 nm (Sullivan et al. 2019). Since we performed chemical experiments instead of field measurements or burn experiments, there is no absorption contribution from black carbon in our chamber. Thus, we can describe total absorption at 405 nm as BrC absorption.

Measurements of gas-phase and particle phase composition of oxygenated compounds were performed by the FIGAERO HR-ToF I^- CIMS (Filter Inlet for Gases and Aerosols High Resolution Time-of-Flight Iodide-Adduct Chemical Ionization Mass Spectrometer), which will hereafter be referred to as the FIGAERO-CIMS (Lee et al. 2014; Lopez-Hilfiker et al. 2014). The

FIGAERO-CIMS has two operating modes switching one after the other: gas-phase mode and particle-phase mode. In gas-phase mode, gases are measured with the I^- CIMS while concurrently in a separate inlet, particles are being collected on a Teflon filter. This mode ran in 10-minute increments with background gas-phase measurements being conducted every 2 minutes to quantify the signal originating from the ion-molecule reaction (IMR) region. In particle-phase mode, heated UHP nitrogen gas is pulled through the particle-laden filter to be sampled by the I^- CIMS. The nitrogen's temperature slowly increases from 20 degrees Celsius to 200 degrees Celsius at a rate of 10 degrees Celsius per minute saturating at 200 degrees Celsius. This heating evaporates compounds with different volatilities off the filter at different temperatures and is known as thermal desorption. The thermal desorption is followed by a 10-minute cooldown period prior to starting the next sampling cycle. The particle-phase mode ran in 60-minute increments where every fourth particle desorption was a particle blank, where a filter is placed upstream of the FIGAERO filter such that no particles are collected during the sampling phase. Particle blanks were linearly interpolated and subsequently subtracted from the normal particle desorption signals. In nitrocatechol's ($C_6H_5NO_4$) case, we assessed what fraction the particle blank contributed to the total particle-phase signal and subtracted that fraction which is not the typical approach and assumes that the magnitude of the blank scales with previous amount of nitrocatechol sampled.

Ionizing flow was set at 2 liters per minute (lpm), chamber sampling flow was 1.5 lpm, particle collection flow was manually set depending on chamber particle loads, IMR-zeroing flow was 2 lpm, and filter desorption flow was 1.8 lpm. Corrections for water vapor interference and dilution were applied in both gas- and particle-phase mode when necessary. The raw data was processed using the Tofware software program (version 3.2.0, Tofwerk AG, Switzerland) running in the Igor Pro 7 programming environment (Wavemetrics, OR, US). Further processing was performed with custom MATLAB scripts (The MathWorks, Inc., MA, US). When sensitivity values for individual compounds were available, they were applied to convert from units of normalized counts per second (ncps) or counts to mixing ratios and mass concentrations. We applied a sensitivity value of 11.8 ncps/ppt to particle-phase nitrocatechol, 4.6 ncps/ppt to gas-phase nitrocatechol, and 12.2 ncps/ppt to gas-phase catechol with water-vapor corrections. All sensitivities have a calibration uncertainty of 30%. When a compound's sensitivity was not known, an empirical value of 5 ncps/ppt was used.

2.3. SOA Yield and Volatility

The SOA mass yield, Y, is defined as the mass concentration of the newly formed organic aerosol (ΔC_{OA}) divided by the mass of the reacted VOC (ΔVOC). In these experiments, ΔC_{OA} is determined with wall-loss corrected OA measurements from the AMS and ΔVOC is estimated with the gas-phase measurements from the FIGAERO-CIMS. The wall-loss correction was implemented by finding the decay rate of the bulk AMS sulfate aerosol in each experiment and adding the lost OA mass back to the baseline measurements. Since the ammonium sulfate dry aerosol seed was the only source of sulfate aerosol in the chamber, the decay of sulfate aerosol as measured by the AMS is solely due to wall loss. We can quantify the molar yield of individual compounds, Y_i, by dividing the observed change in the molar concentration of the product by the change in the molar concentration of the reactant.

Summarizing from earlier, the FIGAERO-CIMS collects particles on a Teflon filter and then desorbs the material collected by increasing the temperature of the UHP nitrogen gas flowing through the filter. Continuously measuring the signal as a function of mass-to-charge during the temperature-varying desorption produces thermograms, the detected signal of compounds as a function of the desorption temperature. The thermogram is a measure of a compound's propensity to evaporate from the collected particles as a function of temperature, and thus is directly related to effective volatility. The temperature at which the desorption signal reaches a maximum is denoted as T_{max}. This property has previously been found to correlate with a compound's enthalpy of sublimation and saturation vapor pressure for approximately ideal mixtures (Lopez-Hilfiker et al. 2014). Thus, we use T_{max} to provide an estimate of volatility independent of the absolute evaporation rate. This method requires proper calibration of the FIGAERO-CIMS, typically conducted by desorbing a broad array of compounds with well-defined enthalpies of sublimation and ensuring the desorption profiles' reproducibility. Calibration experiments conducted with different FIGAERO-CIMS units have shown that one cannot use the same calibration curve for every unit, as the results vary considerably (Bannan et al. 2019; Stark et al. 2017). This variability can be due to differing calibration delivery methods and how compounds are desorbed from the filter, most recently with Ylisirniö et al. (2021) promoting the atomization of calibrant compounds. Additionally, the conditions used to calibrate the FIGAERO-CIMS need to be comparable to those of the environment under investigation (Thornton et al. 2020). Conditions within the NCAR chamber for MOONLIGHT are outside of the FIGAERO-CIMS calibration conditions and any quantitative values derived from the thermograms need to be interpreted with caution. Before T_{max} was evaluated, the thermograms were smoothed with a moving average of 20 seconds and the sample rate was decreased by a factor of 5 to reduce noise.

While T_{max} correlates with enthalpy of sublimation and saturation vapor pressure, it does not perfectly predict these properties without proper calibration and given non-idealities likely in realistic organic aerosol systems. The quantities derived from T_{max} or the whole thermogram reflect the convolution of various properties or processes that affect evaporation such as viscosity and chemical bonding networks. With the aid of a theoretical evaporation model framework designed to interpret FIGAERO-CIMS data, we can compare our experimental results with the theoretical output. The main goal of this model is to reproduce FIGAERO-CIMS thermograms, modeling both the desorption of the compounds from particles on the filter as well as the transport of desorbed vapors through the filter into the ionization region. The desorption model uses a modified Hertz-Knudsen equation as follows,

$$k_{evap,i}[\text{molecules s}^{-1}] = -\frac{1}{\sqrt{2\pi k_B m_i T}}\left(p_i^* \chi_i \alpha \Gamma S\right) \tag{4}$$

where for each compound i, k_B is the Boltzmann constant, m is the molecular mass, T is temperature, p^* is the saturation vapor pressure, χ is a factor accounting for Raoult's law, α is the evaporation coefficient, Γ is a term to correct for gas-phase diffusion limitations, and S is the surface area of the particles on the filter. The transport portion of the model evaluates interactions between the desorbed compounds and the filter and FIGAERO inlet surfaces. This model operates as a function of particle size and is constrained by the same FIGAERO calibration method described earlier. This model is more thoroughly described in Schobesberger et al. (2018).

A variety of group-contribution methods exist to predict pure component vapor pressures of organic compounds serving as measurements of compound volatility. In Myrdal and Yalkowsky (1997), the vapor pressures of 300 diverse organic compounds at 298 K were collected to evaluate their vapor pressure equation, which involves the boiling point, T_b, melting point, T_m, molecular symmetry, σ, the effective number of torsional bonds, τ, and hydrogen bond number, HBN. The equation is provided below as,

$$\log P = -\frac{[56.5-19.2\log(\sigma)+9.2\tau](T_m-T)}{19.1T} - \frac{[86.0+0.4\tau+1421HBN](T_b-T)}{19.1T}$$

$$+\frac{[-90.0-2.1\tau]}{19.1}\left(\frac{T_b-T}{T} - \ln\frac{T_b}{T}\right) \quad (5)$$

Of the 300 organic compounds used to perfect equation 5, three were nitroaromatics: nitrobenzene, 2,6-dinitrotoluene, and 3-nitroaniline, none containing a hydroxyl group. In a separate method, Nannoolal et al. (2008) utilized more than 1600 compound vapor pressure measurements and over 200 chemical groups to perfect their method, which relies on the normal boiling point temperature, T_b, group contributions, dB, and group interactions, GI.

$$\log P = (4.1012+dB)\left(\frac{\frac{T}{T_b}-1}{\frac{T}{T_b}-(1/8)}\right) \quad (6)$$

$$dB = \left(\sum_i N_i C_i + GI\right) - 0.176055 \quad (7)$$

$$GI = \frac{1}{n}\sum_{i=1}^{m}\sum_{j=1}^{m}\frac{C_{i-j}}{m-1} \quad (8)$$

In equations 7 and 8, N_i is the number of groups of type i and C_i is the group contribution of group i. This equation improves upon the Myrdal and Yalkowsky (1997) method by only requiring knowledge of the molecular structure and normal boiling point temperatures. Of the 1600 compounds used to derive equations 6, 7, and 8, thirteen were nitroaromatic. The EVAPORATION method (Estimation of VApour Pressure of Organics, Accounting for Temperature, Intramolecular, and Non-additivity effects) was developed by Compernolle et al. (2011) and only requires molecular structure for vapor pressure computation. Their method is based on the formula,

$$\log P = A + \frac{B}{T^{\kappa}} \qquad (9)$$

where A is a term directly related to the entropy of boiling (ΔS_b) at 1 atm total pressure, $A = \frac{\Delta S_b}{\kappa \ln(10) R}$, and B is a term directly related to the enthalpy of vaporization (ΔH_v), $B = -\frac{\Delta H_v \, T^{\kappa-1}}{\kappa \ln(10) R}$, where κ is a parameter of temperature dependence, T is temperature, and R is the gas constant. These terms can be divided into a sum of group contributions where $A = \sum_k c_k a_k$ and $B = \sum_k c_k b_k$ with c_k as the values of a set of molecular descriptors such as the number of certain functional group in a molecule. They also consider non-additive behavior in the A term for multifunctional compounds. No nitroaromatic compounds were used to create EVAPORATION.

SIMPOL.1, the simplified liquid vapor pressure, p_L^o, prediction method was developed by Pankow et al. (2008). SIMPOL.1 was optimized using nonlinear regression on 456 compounds, including 32 nitro-containing compounds where 25 of those also contained aromatics, and 31 chemical groups. A compound's vapor pressure is determined by calculation of the following,

$$\log p_{L,i}^{o}(T) = v_{0,i} b_0(T) + \sum_k v_{k,i} b_k(T) \quad k = 1, 2, 3\ldots \qquad (10)$$

where $v_{0,i} \equiv 1$ for all compounds, i, $b_0(T)$ is the temperature-dependent coefficient for the zeroth group, k is the group number, and $v_{k,i}$ is the number of k groups on compound i. b_k can be described as follows,

$$b_k(T) = \frac{B_{1,k}}{T} + B_{2,k} + B_{3,k} T + B_{4,k} \ln T \qquad (11)$$

where the numbered B coefficients were solved for and are provided by the SIMPOL.1 method.

The Myrdal and Yalkowsky, Nannoolal, and EVAPORATION vapor pressure estimations for individual compounds were computed with the University of Manchester's UManSysProp: Multiphase system online property prediction tool (http://umansysprop.seaes.manchester.ac.uk/tool/vapour_pressure). Users can specify compounds with SMILES strings, provide an environmental temperature, and indicate the vapor pressure and boiling point methods used. The boiling point methods used for this study were the Joback and Reid (1987) method, Stein and Brown (1994) method, and the Nannoolal (2004) method. SIMPOL.1's calculation of the volatility of nitrocatechol, the dominant compound in all of the catechol experiments, was done in three ways as Pankow et al. (2008) does not explicitly define how a compound like nitrocatechol is to be treated. The authors indicate the use of a nitrophenol group, but not how the other hydroxy group is to be summed and included. The first method does not use the nitrophenol group in its calculation, the second method uses one nitrophenol group in its calculation, and the third method uses two nitrophenol groups in its calculation. Only the low and high volatility values from this calculation are included in analysis hereafter. We emphasize that all group-contribution methods used for this research heavily lack representation from functionalized nitroaromatic compounds.

As a final tool to measure volatility, we utilized gas-particle partitioning theory by implementing two parts of equation 3. The FIGAERO-CIMS gas-phase and particle-phase mass concentrations were used directly to calculate particle-phase fraction defined by C_i^p and C_i^g. In the final part of equation 3, C_{OA} is represented by AMS OA mass concentration as the total absorbing medium and we prescribed different C^* to generate a range of predicted particle-phase fractions for each OA measured in the experiments.

There are limitations in each saturation vapor pressure estimation method as discussed by Lopez-Hilfiker et al. (2014; 2015; 2016) and Stark et al. (2017). These studies show that applying group-contribution methods to all measured compositions shifts the inferred volatility high due to many of the measured compounds being from thermal decomposition of lower volatility components in the SOA (Lopez-Hilfiker et al. 2015; Lopez-Hilfiker et al. 2016). Additionally, Stark et al. (2017) found that using measurements to calculate gas-particle partitioning can result in a skewed volatility distribution, due to signal-to-background limits of instruments, which will vary for each compound and instrument. Lastly, these studies have shown that volatility estimations using the thermal desorptions are reproducible across instruments and are likely the closest to the truth.

Chapter 3. RESULTS AND DISCUSSION

3.1. SOA Yields

SOA mass yields and molar yields for nitrocatechol ($C_6H_5NO_4$) are summarized in **Table 2** and **Table 3**, respectively. Our SOA yields for each catechol-oxidant pair experiment range from 0.38 to 1.63, which are lower than those reported previously (Finewax, de Gouw, and Ziemann 2018). Finewax et al. (2018) report yields ranging from 1.11 to 1.61. These differences could be caused by a few phenomena. While we can correct for loss of particles to the wall, gases can also be lost to the wall. Loss of our gas-phase catechol to the walls likely occurred in the chamber, however in our experiments, an average of 1.5 hours passed after final catechol injection before either the lights turned on or injection of NO_2 occurred, longer than the reported time scale for reaching gas-wall partitioning equilibrium of 7–13 minutes from Krechmer et al. (2016). Finewax et al. (2018) used dioctyl sebacate (DOS) seed aerosol instead of ammonium sulfate seed aerosol. It is possible that having the added organic absorbing medium in the seed enhances yields compared to having an inorganic seed (Song et al. 2011). The Finewax et al. (2018) study also differed in the amounts of reacted catechol and NO_x, reacting up to 56 times more catechol than our experiments and up to 100 times more NO_x. Our amounts of catechol and NO_x within the NCAR chamber are more atmospherically relevant, mimicking the amounts measured in wildfire smoke. Additionally, in some experiments, OA mass may have been produced on particle sizes larger than can be detected by the AMS. The AMS is approximately a PM_1 instrument, not transmitting particles much larger than 1 μm, but the size distributions of the catechol + O_3 + NO_3 experiments as reported by Garofalo et al. (submitted) show sharp increases right near this size cutoff. An estimate of the missing mass was not performed at this time. The FIGAERO-CIMS measured particulate nitrocatechol alone to be as high as 110 μg sm$^-$

^{3} on the 06/14 date, roughly three times higher than the AMS OA mass concentration. Using this value instead, our SOA yield becomes 1.34, within the Finewax et al. (2018) findings. It should be noted that Finewax et al. (2018) measured the SOA mass concentration by weighing aerosol samples collected on pre-weighed filters.

The molar yields of nitrocatechol vary significantly across experiments and within experiments, with maximum molar yields as low as 0.03 in the catechol + OH/NO_x experiment and as high as 1.19 in the catechol + O_3 + NO_3 experiment. Competitive branching and subsequent photochemical losses of nitrocatechol in the OH experiments likely cause the lower inferred molar yield compared to the NO_3 experiments. The highest molar yield occurred on the 06/22 catechol + O_3 + NO_3 dark extended experiment, which was conducted solely in the dark without photochemical aging. While it is physically impossible to have a molar yield greater than 1, the value indicates that realistically, near molar yields of unity occurred. The relative calibration uncertainty combined with uncertainties in wall partitioning can likely account for the higher than unity molar yield.

Date (mm/dd/yyyy)	Oxidant type	Reacted catechol (μg sm^{-3})	AMS SOA peak (μg sm^{-3})	AMS SOA peak wall-loss corrected (μg sm^{-3})	SOA yield	SOA yield wall-loss corrected
06/03/2019	OH	81	26	30	0.32	0.38
06/04/2019	NO_3	26	28	36	1.07	1.38
06/05/2019	NO_3	90	41	52	0.46	0.58
06/14/2019	NO_3	82	38	46	0.46	0.56
06/22/2019	NO_3	35	39	57	1.12	1.63

Table 2. SOA yields for all catechol oxidation experiments.

Date (mm/dd/yyyy)	Oxidant type	Reacted catechol (moles sm^{-3})	Produced nitrocatechol ($C_6H_5NO_4$; moles sm^{-3})	Nitrocatechol ($C_6H_5NO_4$) molar yield
06/03/2019	OH	7.3e-7	2.4e-8	0.03
06/04/2019	NO_3	2.4e-7	2.0e-7	0.86
06/05/2019	NO_3	8.1e-7	5.3e-7	0.65
06/14/2019	NO_3	7.4e-7	7.3e-7	0.99
06/22/2019	NO_3	3.1e-7	3.7e-7	1.19

Table 3. Molar yields of nitrocatechol for all catechol oxidation experiments.

3.2. Gas and Particle Composition of Catechol Oxidation

The gas-phase compounds contributing the most signal for the catechol + OH/NO_x and catechol + O_3 + NO_3 extended experiments are shown in **Figure 1**. For the catechol + OH/NO_x experiment on the top in **Figure 1**, as gas-phase catechol ($C_6H_6O_2$) finished reacting away, nitrocatechol ($C_6H_5NO_4$), the first-generation product expected in high yield, does not substantially increase in the gas-phase. There are some other gas-phase products all with a carbon number of 4, such as $C_4H_{10}O_3$, $C_4H_6O_4$, and $C_4H_9NO_4$, that increase within fifteen minutes of catechol oxidation starting and continues to increase after catechol is depleted indicating multigeneration behavior. The fact that these compounds have a carbon number less than catechol suggests that aromatic ring opening followed by C-C bond scission is occurring over time. The Master Chemical Mechanism v3.3.1 hosted by the University of York (http://mcm.york.ac.uk/home.htt) shows ring opening occurring with catechol + O_3, which does grow in after lights on (see Appendix A). Other nitro-containing compounds such as $C_6H_5NO_3$ and $C_4H_9NO_5$ build up in the chamber over time. CH_2O_2, likely formic acid, additionally continues to grow over time. For the catechol + O_3 + NO_3 extended experiment depicted on the bottom in **Figure 1**, gas-phase catechol is continuously depleted in the chamber while gas-phase nitrocatechol decreases at a much slower rate. Some early generation compounds are ring-opening products $C_4H_9NO_4$ and $C_4H_8O_4$, increasing 1–2 orders of magnitude in 2 hours. Other late-generation compounds were identified such as CH_2O_2, $C_3H_4O_3$, and $C_4H_6O_4$. Gas-phase compounds such as $C_4H_9NO_4$ and $C_4H_{10}O_3$ do not grow as fast as in the catechol + OH/NO_x experiment, perhaps due to less overall O_3 in the chamber or less catechol around once the lights are finally turned on.

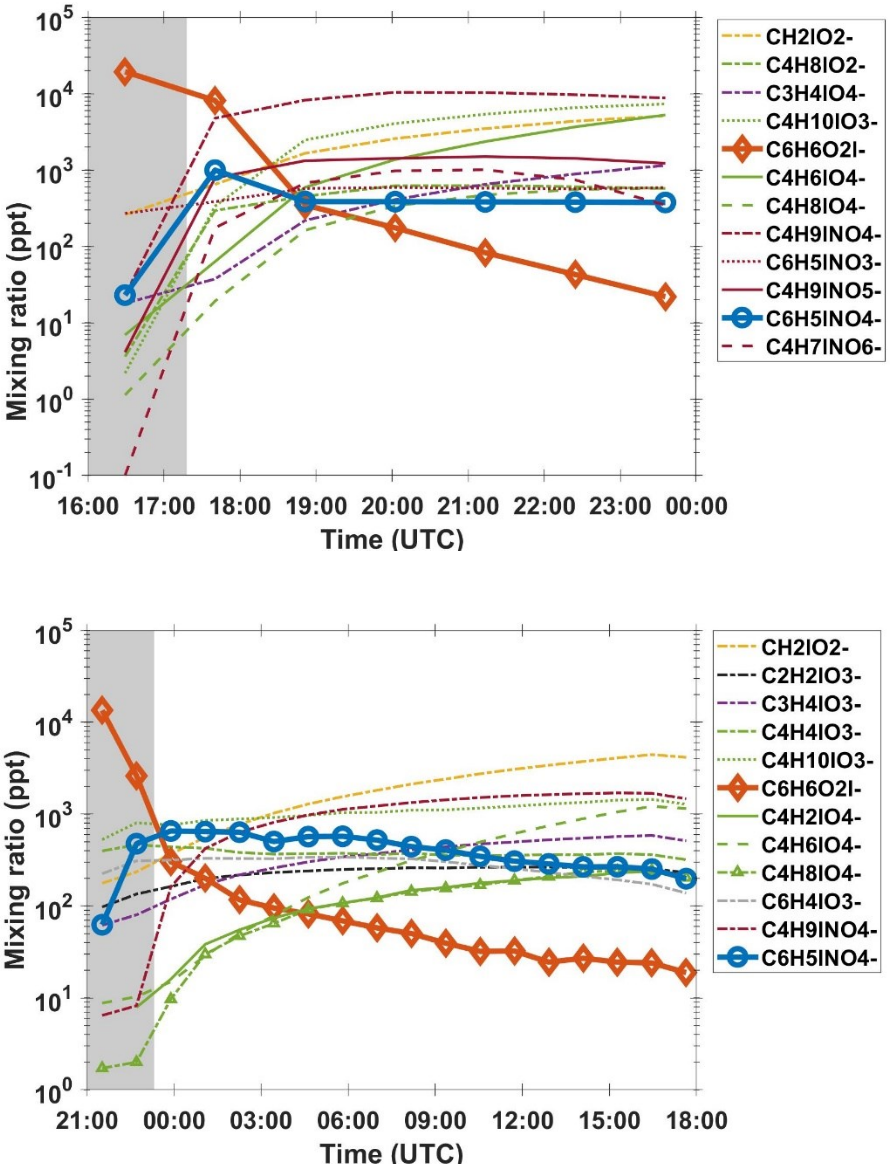

Figure 1. Time series of the notable increasing gas-phase compounds in two experiments. Left: The catechol + OH/NO_x experiment. Right: The catechol + O_3 + NO_3 extended experiment. Grey shading indicates when the lights were off. Organics other than nitrocatechol ($C_6H_5NO_4$) and catechol ($C_6H_6O_2$) are colored by carbon number, while nitrogen-containing compounds are all colored maroon.

The particle-phase compounds contributing the most signal for the catechol + OH/NO_x and catechol + O_3 + NO_3 extended experiments are shown in **Figure 2**. For the catechol + OH/NO_x experiment on the top in **Figure 2**, most of the particle-phase signal from the FIGAERO-CIMS is $C_6H_5NO_4$, presumably that of nitrocatechol, which increases after the lights turn on and release OH and NO bound to H_2O_2 and HONO. Net production of nitrocatechol ceases when catechol is consumed and subsequently decreases over time for the rest of the experiment during which the chamber UV-Vis lights remained on to continue producing OH radicals. In **Figure 3**, we show that 28% of the OA measured by the FIGAERO-CIMS at peak signal is nitrocatechol with limited contributions from other nitro-compounds, apparent accretion products having a number of C greater than that of catechol (C>6), and highly-oxygenated organics. Other organic compounds individually contribute less than 2% of the mass at peak OA signal. For the catechol + O_3 + NO_3 extended experiment on the bottom in **Figure 2**, nitrocatechol is the dominant compound present in the chamber for the entire experiment, as also demonstrated in **Figure 3**, going from contributing 79% of OA at peak FIGAERO-CIMS signal to 62% of OA right before the end of the experiment (not shown). Other contributors to OA mass at the end of the experiment included oxygen number four (O4) compounds such as $C_4H_4O_4$, $C_6H_4O_4$, $C_6H_6O_4$, $C_6H_{10}O_4$, $C_8H_{14}O_4$ as well as other nitrogen-containing compounds. While particulate nitrocatechol slowly decays over the course of the experiment, carbon number six (C6) particulate compounds are produced quickly at the start of the experiment and lose most of their mass after only four hours.

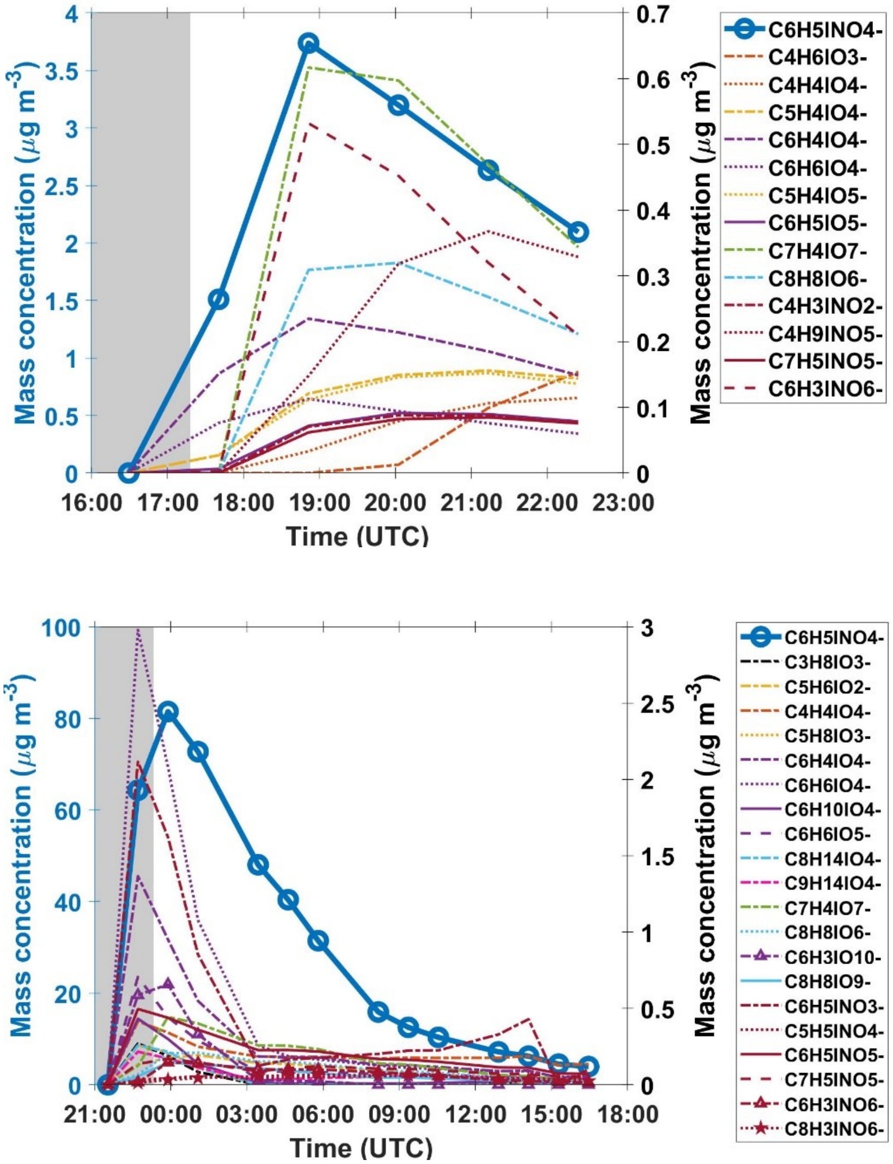

Figure 2. Time series of the notable particle-phase compounds in two experiments. Top: The catechol + OH/NO$_x$ experiment. Bottom: The catechol + O$_3$ + NO$_3$ extended experiment. Nitrocatechol ($C_6H_5NO_4$) is plotted on the blue left y-axis for both plots and all other compounds are plotted on the black right y-axis. Grey shading indicates when the lights were off. Organics are colored by carbon number, while nitrogen-containing compounds are all colored maroon, excluding nitrocatechol ($C_6H_5NO_4$).

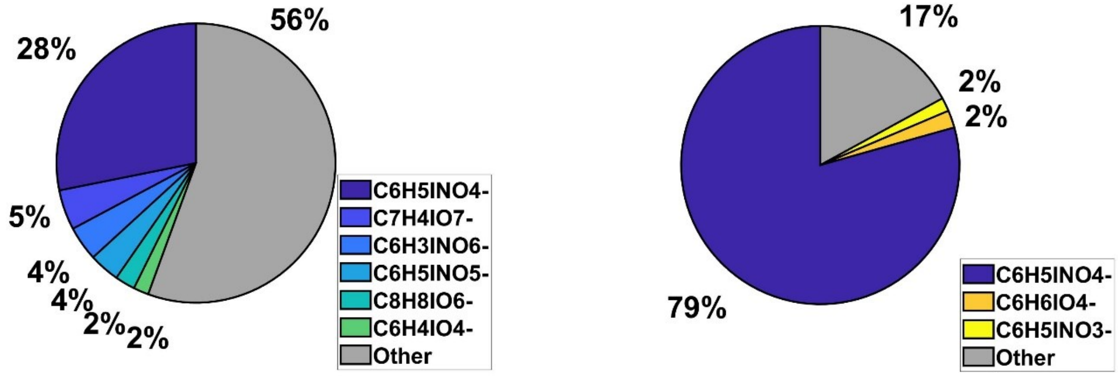

Figure 3. The OA composition for the two experiments at peak OA signal. Left: Catechol + OH/NO_x experiment. Right: Catechol + O_3 + NO_3 extended experiment.

3.3. Observed Thermogram Properties and Evolution

The FIGAERO-CIMS thermogram for a single compound in an ideal liquid solution will be a single near-Gaussian peak with a fixed T_{max} (Lopez-Hilfiker et al. 2014; Schobesberger et al. 2018). However, this behavior is not often the case, especially in complex SOA where some compounds have multiple peaks, some may have broad high temperature (low volatility) peaks, and experimental conditions (such as the amount of aerosol on a filter) can vary altering the slope of the initial rising signal and T_{max} as properties of the SOA vary. Investigations into the thermograms of nitrocatechol produced in the 06/14 catechol + O_3 + NO_3 extended experiment reveal that the volatility of nitrocatechol dramatically shifts after the first desorption, shown in **Figure 4**. This shift is not apparent in the other experiments as we typically sampled aerosol only when a substantial amount of OA was detected by the AMS. This sampling was done to avoid missing early chemistry as the FIGAERO-CIMS has a long duty cycle (1 hour vs minutes of starting chemistry). The T_{max} jumps from 80 ºC to roughlt 110 ºC, equivalent to a three-order magnitude decrease in saturation concentration (e.g., 10^{-1}–10^{-4} μg m^{-3}) all else the same. The absolute signal in a thermogram, shown on the left in **Figure 4**, decreases to its original value before the experiment end, but the nitrocatechol T_{max} does not shift back to its original value of

~80 ºC. Thus, the shift to higher T_{max} over the course of the experiment is not due to differences in compound mass loading, as more mass collected on a filter leads to an increase in T_{max} (Huang et al. 2018). This behavior implies that the effective volatility of $C_6H_5NO_4$ is decreasing with particle aging perhaps due to changing physical phase state, and/or other low volatility components are decomposing during the high temperature portion of the thermogram to produce a nitrocatechol. In addition, the signal associated with the higher-temperature tail of the thermogram increases relative to that at the T_{max} over time, first after the nitrocatechol absolute signal starts decreasing and then again towards the end of the experiment, evident on the right in **Figure 4**.

As time progresses, the differences in normalized thermogram area normalized by AMS sulfate aerosol (SO_4) integrated between 0 to 110 ºC and 110 to 200 ºC increase after 09:00 UTC as seen in **Figure 5**. Such behavior is observed in other SOA systems, such as that from monoterpenes, and has been connected to accretion chemistry of particle-phase components into oligomer networks (Lopez-Hilfiker et al. 2015). The average T_{max} for all desorptions following the first is 107.8 ºC or $C^* = 1.8 \times 10^{-4}$ μg m^{-3} when we use the saturation concentration calibration curve derived in Lopez-Hilfiker et al. (2014). Using the Chuang and Donahue (2016) volatility classification scheme, nitrocatechol is an extremely low volatility organic compound (ELVOC), compounds thought to be responsible for the creation of cloud condensation nuclei and new particle formation. With this saturation concentration, in nearly all OA environments, nitrocatechol will exist solely in the particle phase. Additional nitrocatechol thermograms for different experiment days can be found in Appendix B. Figures of the differences in integrated low temperature and high temperature areas of the normalized nitrocatechol thermograms for all other catechol experiments can be found in Appendix E.

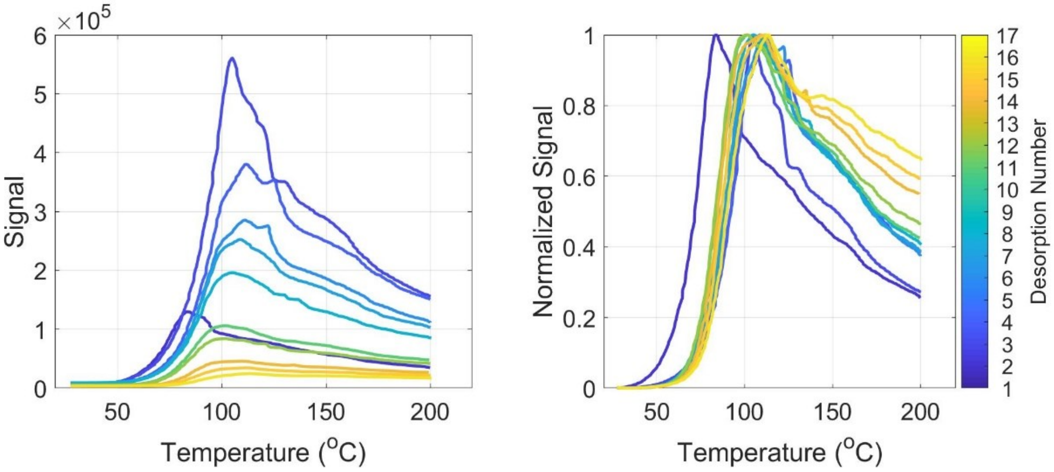

Figure 4. Nitrocatechol thermograms colored by increasing experiment time (increasing desorption number) from blue to yellow since the start of the 06/14 catechol + O_3 + NO_3 extended experiment. Left: Thermogram of absolute signal. Right: Thermogram of normalized signal. Filter blank thermograms are not included in this plot.

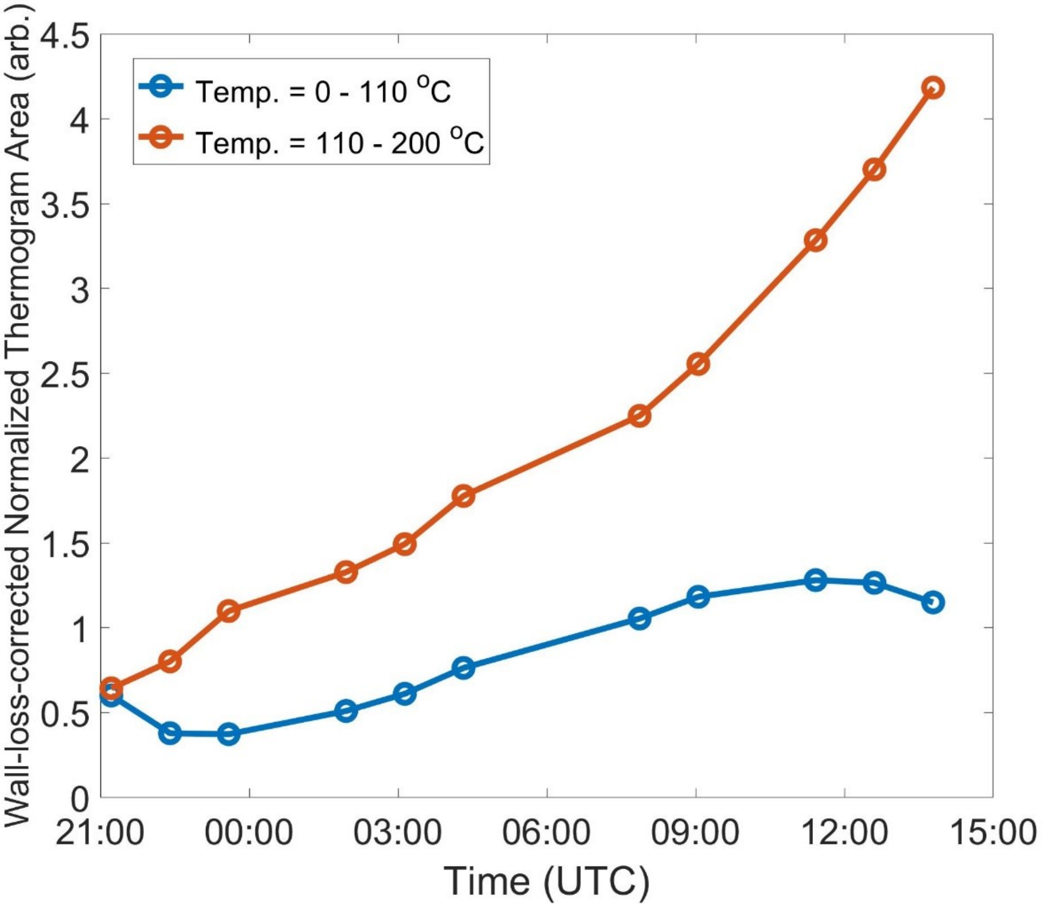

Figure 5. Time series of the integrated normalized nitrocatechol thermograms from Figure 4 with the integrations separated at a temperature of 110 °C and normalized by AMS SO_4 to normalize by chamber wall losses for the 06/14 catechol + O_3 + NO_3 extended experiment.

3.4. Constraints on the nitrocatechol C^*

We observed in section 3.2 that nitrocatechol is the dominant compound produced in all the catechol oxidation experiments. However, being concerned with aerosol evolution and fate, it is also critical to understand the affinity of nitrocatechol for the gas and particle phases. A compound’s lifetime is heavily dependent on phase, dictating reaction rates with other oxidants and well as wet and dry deposition rates (Bidleman 1988). Thus, there is a need for accurate representation of the volatilities of compounds to enhance model predictability. These chamber experiments provided an opportunity to assess the volatility of nitrocatechol as it would exist in atmospherically relevant conditions. Employing the observed and calculated F_p method described in equation 3 for all the catechol experiments results in a volatility estimate depicted in **Figure 6**. The C^* that best matches the 1:1 line is approximately 5 µg m^{-3}, characterizing nitrocatechol as a semivolatile compound. There is some support for a saturation vapor concentration of order 1 µg m^{-3}, but little support for > 50 µg m^{-3}. The "horseshoe" shape of the F_p values is due to each arm being a different catechol + O_3 + NO_x extended experiments. While calibration and instrument precision uncertainties were considered, other systematic uncertainties such as non-ideality and non-equilibrium conditions in the chamber were not.

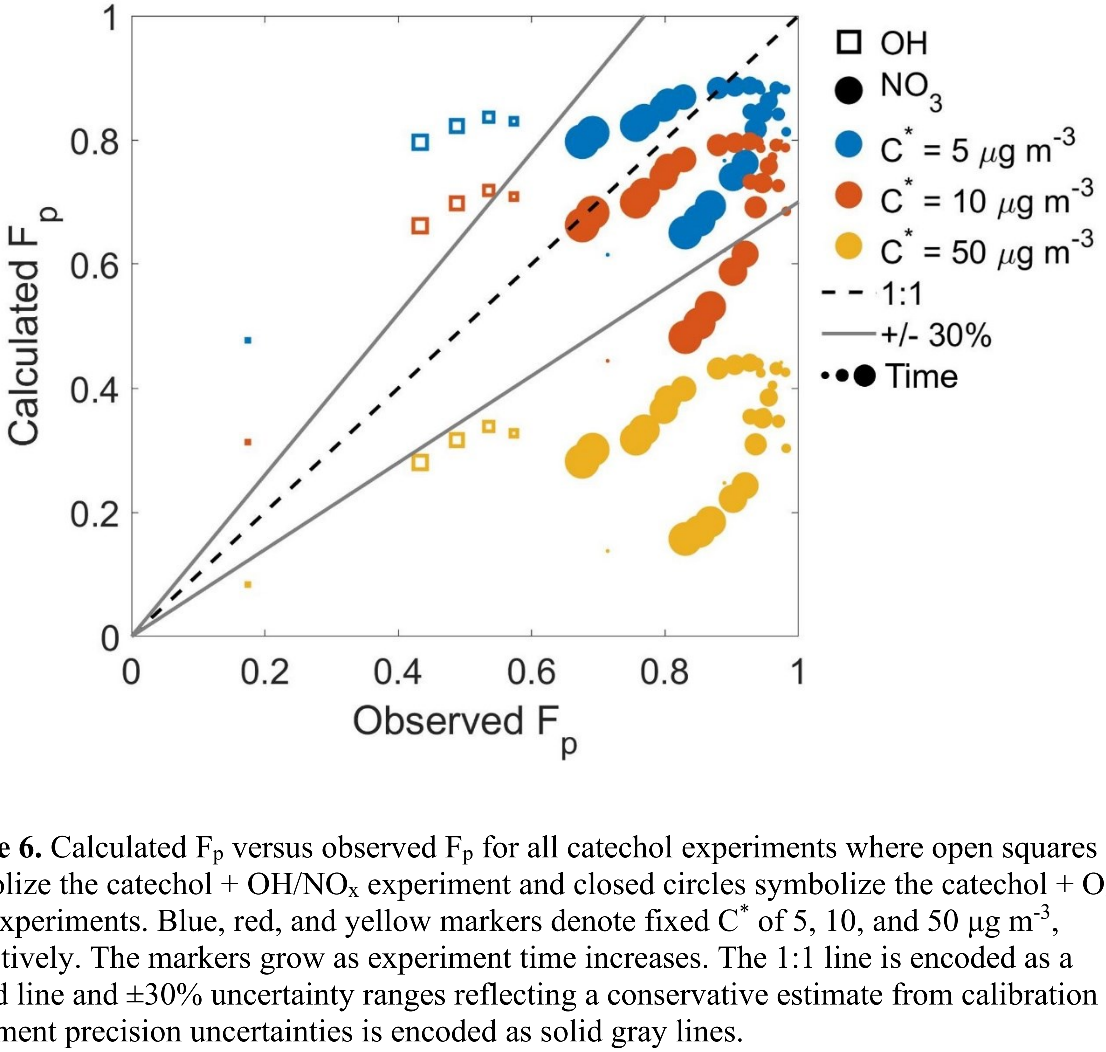

Figure 6. Calculated F_p versus observed F_p for all catechol experiments where open squares symbolize the catechol + OH/NO_x experiment and closed circles symbolize the catechol + O_3 + NO_3 experiments. Blue, red, and yellow markers denote fixed C^* of 5, 10, and 50 µg m^{-3}, respectively. The markers grow as experiment time increases. The 1:1 line is encoded as a dashed line and ±30% uncertainty ranges reflecting a conservative estimate from calibration and instrument precision uncertainties is encoded as solid gray lines.

Compiling all the volatility estimates using group contribution methods, measured gas-particle partitioning, thermal desorption methods, and thermal desorption modeling we find that nitrocatechol volatility ranges from 10^{-5} to 10^{9} µg m^{-3}, 14 orders of magnitude, and from 10^{0} to 10^{9} µg m^{-3} if the FIGAERO-CIMS thermal desorption method is excluded, due to chamber conditions being outside the range of the calibration curve. Figures in Appendix C show in detail the normalized and absolute thermogram signals for the rest of the catechol experiments, all yielding a $C^{*} < 1$ µg m^{-3}. **Figure 7** details how each method varied in nitrocatechol volatility estimates. Our study using the measurement-based gas-particle partitioning method is encoded by the black square at 5 µg m^{-3}. This value is roughly on par with the Finewax et al. (2018) volatility estimate of 13 µg m^{-3} considering the likely order of magnitude uncertainties associated with the methodology and as compared to the wide range of estimates from group contribution methods.

For each of the group contribution methods that use a SMILES string as input, two different SMILES strings sources were used to test the adaptability of the code on UManSysProp, one from the Master Chemical Mechanism (MCM), O=N(=O)c1ccc(O)c(O)c1, and the other from PubChem, C1=CC(=C(C=C1[N+](=O)[O-])O)O. It has been confirmed that while their SMILES strings are different, they result in the same structure of 4-nitrocatechol. When using the MCM SMILES string, the group contribution methods Nannoolal (2008) and Myrdal and Yalkowsky (1997) yield similar volatilities of 3.0 and 12.6 µg m^{-3} respectively. On the other side, the PubChem SMILES string results in higher volatilities by 3 to 4 orders of magnitude, 8.5×10^{4} and 9.2×10^{4} µg m^{-3} in the same respective order. Different SMILES strings had no impact on the EVAPORATION method but had reported the highest volatility of nitrocatechol at 8.5×10^{8} µg m^{-3}. SIMPOL.1 had ranged from 1.8×10^{2} to 2.4×10^{6} µg m^{-3}, with a middle value of 2.1×10^4 μg m^{-3}. Again, it was the lack of clarity on group contribution calculations, specifically whether to use two nitrophenol groups, two aromatic hydroxyl groups, or one of each for the hydroxyl groups, that led to the calculation of these three values. Considering all the volatility estimation methods, nitrocatechol volatility is not easy to pin down. The group contribution methods could have been lacking for this compound due to their paucity of vapor pressure information for nitroaromatic compounds. These group contribution methods would also not be considering other effects such as oligomerization which could have played a role in the FIGAERO-CIMS thermal desorption estimates. Finally, we also acknowledge that signal-to-background limitations are at play in the measurement-based gas-particle partitioning method, but these lead to derived C^* that are biased high, and as such the group contribution methods likely overestimate the nitrocatechol C^* by wide margins.

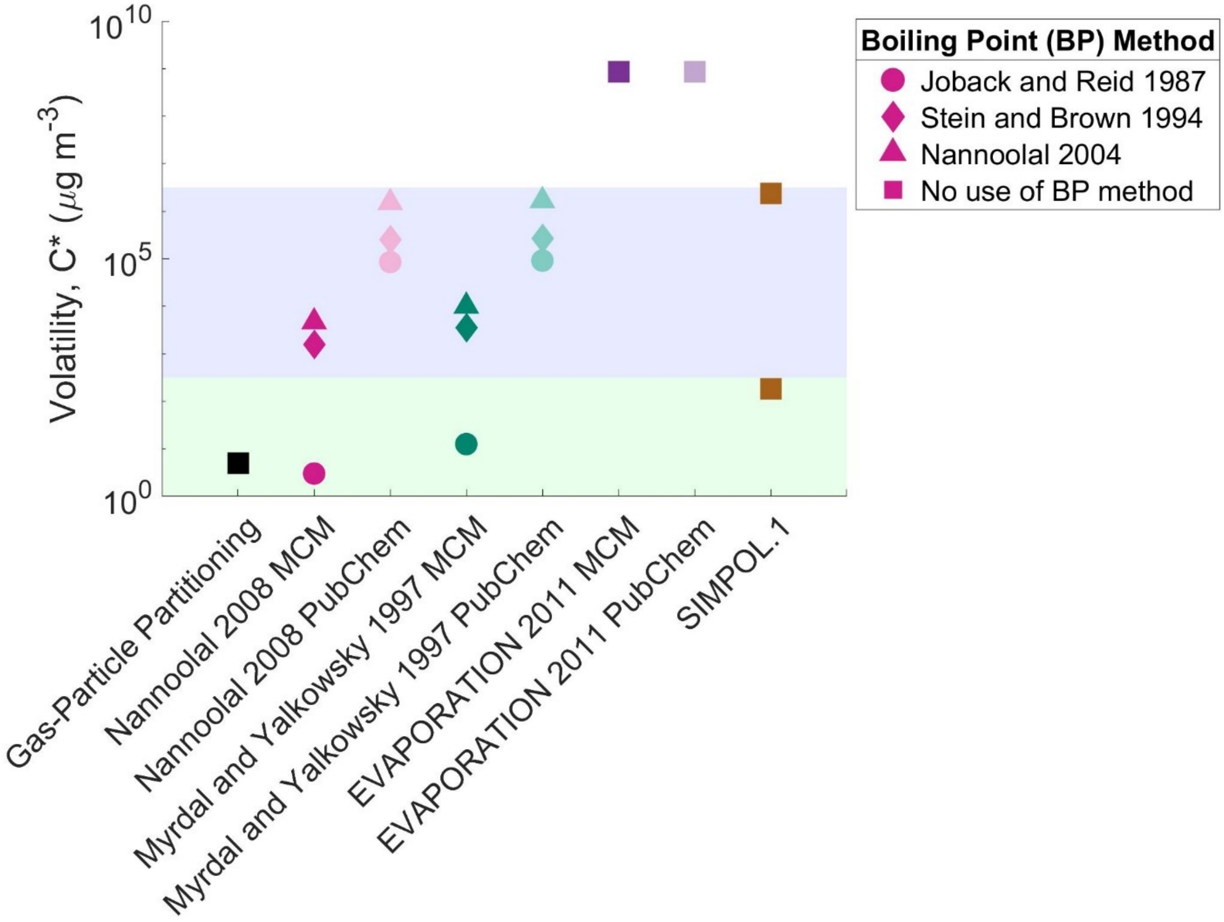

Figure 7. Comparing different C* estimations. Each color of the dots represents a different group-contribution method, with MCM-provided SMILES strings in the darker color and the PubChem-provided SMILES strings in the lighter color. Each shape denotes a different boiling point method used. SIMPOL.1 did not use a SMILES string. Volatility classes are shaded in the background and colored as in Chuang and Donahue (2016).

Comparing our results with the FIGAERO-CIMS theoretical model using the same calibration curve in Lopez-Hilfiker et al. (2014), we found that under the assumption the particles are 2 μm in diameter for the 06/05 catechol + O_3 + NO_3 extended experiment, the volatility of nitrocatechol ($C_6H_5NO_4$) is 1.1 μg m^{-3}, with the model fit illustrated in **Figure 8**. While this model captures the thermogram peak nicely, the single-compound model fails to adequately capture the slope of the low-temperature signal increase as well as the area of the thermogram right after 105 °C. Being able to capture the slope of the low-temperature signal is as critical as capturing the temperature at maximum signal as volatility is a temperature-dependent quality. Current evaporative theory should be able to model a thermogram at all temperatures. Although it would be better to capture the entire behavior of the thermogram, adding more compound desorption peaks does not add information about nitrocatechol specifically. Additionally, there is no way to verify that the compounds added to improve the fit are real and are at the right volatilities. Unfit thermogram area right after 105 °C indicates that the thermogram for $C_6H_5NO_4$ is not consistent with a single compound evaporating from an ideal mixture without diffusion limitations. That is, the single-compound model is missing roughly half of the thermogram mass mostly in the high-temperature tail consistent with other very low volatility compounds decomposing into nitrocatechol ($C_6H_5NO_4$) or that the phase state or morphology of particles is restricting evaporation of nitrocatechol.

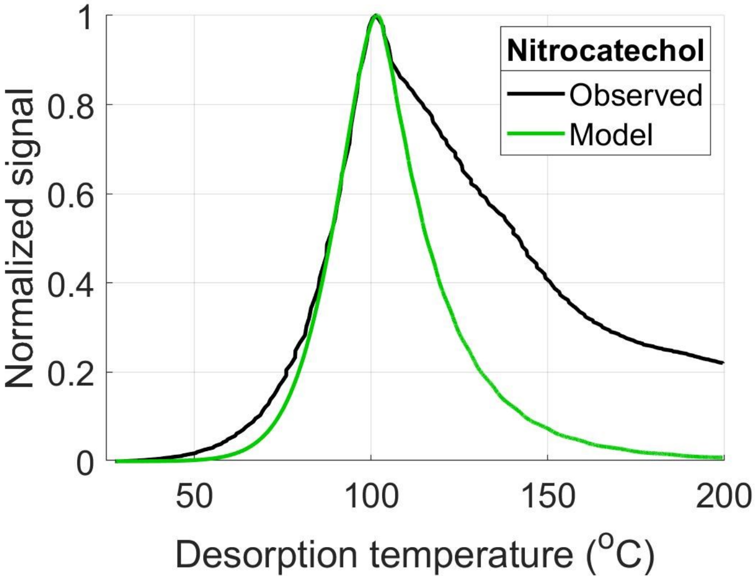

Figure 8. Fit of the catechol + O_3 + NO_3 nitrocatechol's ($C_6H_5NO_4$) first thermogram. Observational data is encoded as a black line while the model fit is encoded as a green line.

3.5. Evolution of particulate absorption

Nitrocatechol is one of the nitroaromatics that comprises BrC. Here we examine the extent to which the evolutions of nitrocatechol and UV-Vis absorption are related to connect changes in BrC such as photobleaching, to subsequent chemistry of nitrocatechol. We showed earlier that particle-phase nitrocatechol is a major or dominant compound in both the catechol + OH/NO_x and the catechol + O_3 + NO_3 experiments. In **Figure 9**, the evolution of PAS absorption at 405 nm, AMS OA, and particle-phase nitrocatechol during the catechol + OH/NO_x experiment are shown. The absolute AMS OA and particle-phase nitrocatechol follow a similar trend as the PAS absorption, but the particle-phase nitrocatechol follows absorption more closely: the particle-phase nitrocatechol peaks at the same time as the PAS absorption and follows more closely the decay in measured light absorption. Normalizing these measurements by the AMS SO_4 shown on the right in **Figure 9**, accounts for loss of particles to the chamber walls. After 21:00 UTC, the AMS OA stays roughly constant, indicating that no net OA is being formed or lost while particle-phase nitrocatechol continues to closely follow the light absorption decay. As particle-phase nitrocatechol accounts for most of the FIGAERO-CIMS speciated OA mass concentration, we conclude it is the compound driving particle light absorption.

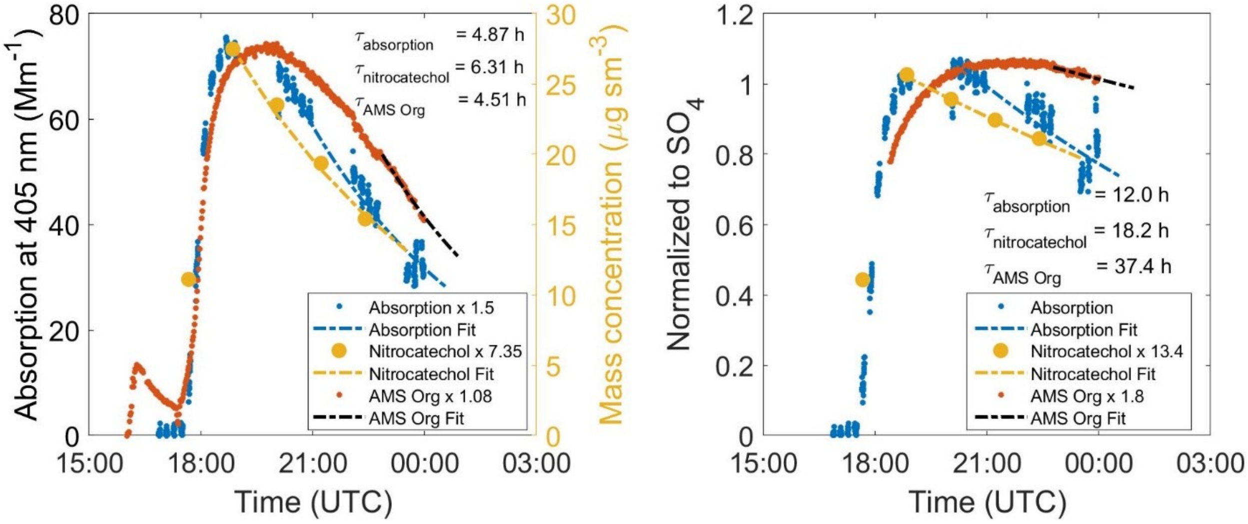

Figure 9. The 06/03 catechol + OH/NO$_x$ experiment. Left: Time series of the absorption as measured by the PAS at 405 nm and mass concentrations of AMS OA, and particle-phase nitrocatechol. Right: The same measurements normalized by AMS SO$_4$. Some data have been multiplied by factors to compare the shapes of the different curves. Exponential decay fits of each variable are plotted as dashed lines. Lifetimes, τ, of these fits are reported in the figure text.

Comparing the evolution of nitrocatechol, absorption at 405 nm, and AMS OA for the 06/05 catechol + O$_3$ + NO$_3$ extended experiment reveals that the absorption follows the absolute particle-phase nitrocatechol and not AMS OA, as shown on the left in **Figure 10**. Wall-loss corrected particle-phase nitrocatechol closely follows the decay in light absorption even though AMS total OA changes relatively little after 06:00 UTC. Even more so in this experiment, the FIGAERO-CIMS OA was composed primarily of nitrocatechol, thus we can attribute the absorption to nitrocatechol. A similar time series figure for the 06/14 catechol + O$_3$ + NO$_3$ experiment can be found in Appendix C. A closer look at the differences in AMS OA trends and FIGAERO-CIMS OA trends can be found in Appendix D.

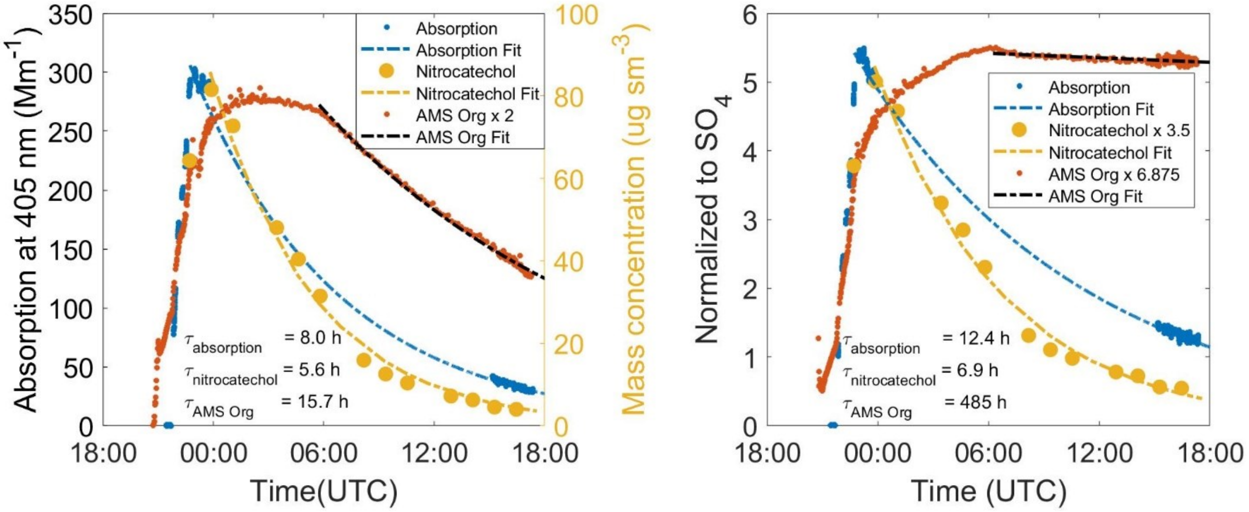

Figure 10. Similar to **Figure 9**, but for the 06/05 catechol + O_3 + NO_3 extended experiment. Left: Absolute measurements. Right: Measurements normalized to AMS SO_4. Some data have been multiplied by factors to compare the shapes of the different curves. Exponential decay fits of each variable are plotted as dashed lines. Lifetimes, τ, of these fits are reported in the figure text.

The lifetime of 405 nm light absorption, our proxy for BrC, normalized to AMS SO_4 is approximately 12 hours in both the 06/03 catechol + OH/NO_x and the 06/05 catechol + O_3 + NO_3 experiments. However, the lifetime of nitrocatechol is roughly three times shorter in the 06/05 catechol + O_3 + NO_3 extended experiment. Due to chamber volume sampling restrictions, we do not have light absorption data overnight that would further confirm the exponential fit. This reduced lifetime of particulate nitrocatechol could indicate particle processing is occurring or it could indicate differences in particle morphology, as the 06/03 catechol + OH/NO_x aerosol was not solely nitrocatechol-dominated. Different compound interactions could be at play. Since light absorption has a slower decay than the decay of nitrocatechol, nitrocatechol is not the only light absorbing compound.

Chapter 4. CONCLUSIONS

MOONLIGHT was an extensive set of chamber experiments conducted with multiple academic and governmental institutions quantifying multiple facets of phenolic and monoterpene reaction experiments, building on discoveries from sampling wildfire smoke during the WE-CAN field campaign. With a specific focus on catechol as a representative wildfire-derived reactive phenolic compound, we investigated the effects that daytime, or OH-initiated, and nighttime, or NO_3-initiated, chemistry had on SOA formation and properties using a FIGAERO-CIMS. We also probed the evolution of this SOA to mimic light-enhanced loss of BrC from authentic wildfire plumes.

Molar yields of nitrocatechol ranged from 0.65 to unity for NO_3-initiated oxidation, and 0.03 for OH oxidation. Maximum SOA mass yields from catechol oxidation were strongly tied to formation of nitrocatechol, ranging from 0.38 to 1.63 for the different experiments, lower than the previously reported values of 1.11 to 1.61 (Finewax, de Gouw, and Ziemann 2018). Higher SOA mass yields from catechol oxidation were found for NO_3 rather than OH oxidation.

In the gas-phase, OH-initiated oxidation of catechol resulted in greater growth of C4 compounds compared to the dark chemistry experiments, indicating a greater propensity for aromatic ring opening during photo-oxidation. Consistent with this finding, while nitrocatechol was a major product in both conditions, dark NO_3-driven chemistry nitrocatechol molar yields reached up to unity. As a result, nitrocatechol explained 79% of measured OA mass formed from NO_3-initiated catechol oxidation while it explained 28% from the (high-NO_x) OH-initiated catechol oxidation. Using gas-particle partitioning theory and measurements, we inferred a nitrocatechol C^* of roughly 5 $\mu g\ m^{-3}$ while the modeled thermograms imply a C^* of 1.1 $\mu g\ m^{-3}$ or lower. It is important to note that various C^* estimation methods predicted a range spanning 8 orders of magnitude in the C^* of nitrocatechol. Depending on the application, nitrocatechol would be treated either as a VOC, an intermediate VOC, or a semivolatile VOC, each with vastly different phase distributions. These methods have real world atmospheric chemistry modeling applications, as EVAPORATION is used in the F0AM-WAM model (D'Ambro et al. 2017) and has also been used with the CMAQv5.2γ model (Pye et al. 2018) and SPectral Aerosol Cloud Chemistry Interaction Model (SPACCIM) (Gatzsche et al. 2017), and SIMPOL.1 is easily coupled to the MCM (Chen et al. 2011; Ruggeri et al. 2016). Limited numbers of nitroaromatics went into the development of these group-contribution methods. Thus, there is a need to revisit C^* estimation methods for oxidized and nitrated aromatic compounds.

Providing insight on the volatility of nitrocatechol allows us to understand its gas-particle partitioning in wildfire smoke, effectively determining which chemical and physical processes have a higher relative importance in determining its fate, like those of aerosol reactions, such as heterogeneous oxidation, versus gas-phase reactions and repartitioning due to dilution. These fates in turn have implications for SOA and BrC formation and loss as plumes age. For example, by assigning nitrocatechol saturation vapor concentration on the order of 10 $\mu g\ m^{-3}$, and assuming typical wildfire OA concentrations of 10 to 1000 $\mu g\ m^{-3}$, gas-particle partitioning theory determines that nitrocatechol will vary from ~50% to 100% in the particle phase. Nitrocatechol in wildfire thick-plume conditions theoretically will partition predominantly into the particle phase based on our results but is still subject to significant dynamic repartitioning upon plume dilution. However, if the volatility evolution observed in the chamber experiments is a guide, then it is likely that phenolic SOA will become less volatile with aging, to the point where wet scavenging by precipitation may become the main atmospheric removal pathway.

Photochemical aging of the SOA, both with and without gas-phase radical scavengers like 2-butanol, led to reduction in nitrocatechol particle mass concentrations, as well as BrC absorption at 405 nm, at rates that exceeded particle wall loss. The BrC light absorption decayed via aging with a lifetime of ~12 hours in both OH- and NO_3-initiated SOA experiments. This is similar to previously reported lifetimes of BrC in transported wildfire smoke (Forrister et al. 2015). However, the observed particulate nitrocatechol decay upon photochemical aging differed, exhibiting a lifetime of roughly 18 hours when formed from OH chemistry and approximately 7 hours from dark chemistry. BrC light absorption measurements occurred only before and after extended aging periods, so we do not have enough information to conclude if the particulate nitrocatechol lifetimes differ significantly from the BrC lifetime.

With photobleaching lifetimes of less than a day, wildfire BrC being photochemically processed in this way will be reduced to 13.5% of its initial absorbance in 24 hours of daylight, potentially 3 days aloft, as most wildfires grow and increase their emissions through the afternoon when temperatures are highest. While the BrC photochemical decay rate did not vary substantially with SOA formation chemistry, that of particulate nitrocatechol did. The different rate of particulate nitrocatechol loss depending upon whether it was formed from OH photochemical or NO_3 dark oxidation of catechol is not yet understood. We propose that differences in particle morphology may play a role. The OH-initiated experiments led to SOA with a more complex composition, where nitrocatechol was not the dominant particle component. Such a situation could lead to reduced rates of evaporation to the gas-phase compared to the SOA formed in the NO_3-initiated experiments, where nitrocatechol was by far the dominant component of the particles (and thus likely the particle surface). Evaluations of nitrocatechol heterogeneous oxidation by OH indicated that this loss pathway was too small to impact nitrocatechol on the timescales we observed in the chamber. In addition, the NO_3-initiated oxidation produced nitrocatechol SOA so efficiently, particles containing most of the nitrocatechol mass likely has sizes in the 1 to 3 μm range (Garofalo et al. submitted). These larger particles potentially have differential settling and wall loss rates compared to the sulfate mass which was distributed in finer particles. Thus, while our measured BrC lifetimes are similar to those found in authentic wildfire plumes, the exact mechanisms driving the evolution of BrC from phenolic compounds oxidation remain unidentified.

Nitroaromatics such as nitrocatechol are not only present in biomass burning smoke but can arise from oxidation of anthropogenic emissions of aromatics associated with fossil fuel use and volatile consumer products (VCP) (McDonald et al. 2018). Nitroaromatics are thus also likely important in urban SOA. Based on our findings it is possible that air quality models may be underestimating an anthropogenic SOA source if not tracking the multi-generational aging of aromatics. In addition, nitroaromatics are used in pesticides, dyes, explosives, pharmaceuticals, and in the chemical synthesis industry, and such knowledge of their C^* will help determine emissions from these potential source categories. Previous research studying the volatility of the aerosol in these urban environments using group contribution methods will likely need to be reevaluated.

REFERENCES

Akagi, S. K., R. J. Yokelson, C. Wiedinmyer, M. J. Alvarado, J. S. Reid, T. Karl, J. D. Crounse, and P. O. Wennberg. 2011. “Emission Factors for Open and Domestic Biomass Burning for Use in Atmospheric Models.” *Atmospheric Chemistry and Physics* 11 (9): 4039–72. https://doi.org/10.5194/acp-11-4039-2011.

Andreae, M. O., and P. Merlet. 2001. “Emission of Trace Gases and Aerosols from Biomass Burning.” *Global Biogeochemical Cycles* 15 (4): 955–66. https://doi.org/10.1029/2000GB001382.

Andreae, Meinrat O. 2019. “Emission of Trace Gases and Aerosols from Biomass Burning – an Updated Assessment.” *Atmospheric Chemistry and Physics* 19 (13): 8523–46. https://doi.org/10.5194/acp-19-8523-2019.

Bannan, Thomas J., Michael Le Breton, Michael Priestley, Stephen D. Worrall, Asan Bacak, Nicholas A. Marsden, Archit Mehra, et al. 2019. “A Method for Extracting Calibrated Volatility Information from the FIGAERO-HR-ToF-CIMS and Its Experimental Application.” *Atmospheric Measurement Techniques* 12 (3): 1429–39. https://doi.org/10.5194/amt-12-1429-2019.

Barbero, R., J. T. Abatzoglou, N. K. Larkin, C. A. Kolden, and B. Stocks. 2015. “Climate Change Presents Increased Potential for Very Large Fires in the Contiguous United States.” *International Journal of Wildland Fire* 24 (7): 892. https://doi.org/10.1071/WF15083.

Bidleman, Terry F. 1988. “Atmospheric Processes.” *Environmental Science & Technology* 22 (4): 361–67. https://doi.org/10.1021/es00169a002.

Bolzacchini, Ezio, Maurizio Bruschi, Jens Hjorth, Simone Meinardi, Marco Orlandi, Bruno Rindone, and Elisa Rosenbohm. 2001. “Gas-Phase Reaction of Phenol with NOq$_3$.” *Environmental Science & Technology* 35 (9): 1791–97. https://doi.org/10.1021/es001290m.

Bond, T. C., S. J. Doherty, D. W. Fahey, P. M. Forster, T. Berntsen, B. J. DeAngelo, M. G. Flanner, et al. 2013. “Bounding the Role of Black Carbon in the Climate System: A Scientific Assessment: BLACK CARBON IN THE CLIMATE SYSTEM.” *Journal of Geophysical Research: Atmospheres* 118 (11): 5380–5552. https://doi.org/10.1002/jgrd.50171.

Boucher, O., D. Randall, P. Artaxo, C. Bretherton, G. Feingold, P. Forster, V.-M. Kerminen, Y. Kondo, H. Liao, U. Lohmann, P. Rasch, S.K. Satheesh, S. Sherwood, B. Stevens and X.Y. Zhang, 2013: Clouds and Aerosols. In: Climate Change 2013: The Physical Science Basis. Contribution of Working Group I to the Fifth Assessment Report of the Intergovernmental Panel on Climate Change [Stocker, T.F., D. Qin, G.-K. Plattner, M. Tignor, S.K. Allen, J. Boschung, A. Nauels, Y. Xia, V. Bex and P.M. Midgley (eds.)]. Cambridge University Press, Cambridge, United Kingdom and New York, NY, USA.

Brown, Steven S., Hyunjin An, Meehye Lee, Jeong-Hoo Park, Sang-Deok Lee, Dorothy L. Fibiger, Erin E. McDuffie, William P. Dubé, Nicholas L. Wagner, and Kyung-Eun Min. 2017. "Cavity Enhanced Spectroscopy for Measurement of Nitrogen Oxides in the Anthropocene: Results from the Seoul Tower during MAPS 2015." *Faraday Discussions* 200: 529–57. https://doi.org/10.1039/C7FD00001D.

Buysse, Claire E., Aaron Kaulfus, Udaysankar Nair, and Daniel A. Jaffe. 2019. "Relationships between Particulate Matter, Ozone, and Nitrogen Oxides during Urban Smoke Events in the Western US." *Environmental Science & Technology* 53 (21): 12519–28. https://doi.org/10.1021/acs.est.9b05241.

Chen, Qi, Yingjun Liu, Neil M. Donahue, John E. Shilling, and Scot T. Martin. 2011. "Particle-Phase Chemistry of Secondary Organic Material: Modeled Compared to Measured O:C and H:C Elemental Ratios Provide Constraints." *Environmental Science & Technology* 45 (11): 4763–70. https://doi.org/10.1021/es104398s.

Chuang, W. K., and N. M. Donahue. 2016. "A Two-Dimensional Volatility Basis Set – Part 3: Prognostic Modeling and NOx Dependence." *Atmospheric Chemistry and Physics* 16 (1): 123–34. https://doi.org/10.5194/acp-16-123-2016.

Compernolle, S., K. Ceulemans, and J.-F. Müller. 2011. "EVAPORATION: A New Vapour Pressure Estimation Methodfor Organic Molecules Including Non-Additivity and Intramolecular Interactions." *Atmospheric Chemistry and Physics* 11 (18): 9431–50. https://doi.org/10.5194/acp-11-9431-2011.

D'Ambro, Emma L., Kristian H. Møller, Felipe D. Lopez-Hilfiker, Siegfried Schobesberger, Jiumeng Liu, John E. Shilling, Ben Hwan Lee, Henrik G. Kjaergaard, and Joel A. Thornton. 2017. "Isomerization of Second-Generation Isoprene Peroxy Radicals: Epoxide Formation and Implications for Secondary Organic Aerosol Yields." *Environmental Science & Technology* 51 (9): 4978–87. https://doi.org/10.1021/acs.est.7b00460.

DeCarlo, Peter F., Joel R. Kimmel, Achim Trimborn, Megan J. Northway, John T. Jayne, Allison C. Aiken, Marc Gonin, et al. 2006. “Field-Deployable, High-Resolution, Time-of-Flight Aerosol Mass Spectrometer.” *Analytical Chemistry* 78 (24): 8281–89. https://doi.org/10.1021/ac061249n.

Dennison, Philip E., Simon C. Brewer, James D. Arnold, and Max A. Moritz. 2014. “Large Wildfire Trends in the Western United States, 1984-2011.” *Geophysical Research Letters* 41 (8): 2928–33. https://doi.org/10.1002/2014GL059576.

Finewax, Zachary, Joost A. de Gouw, and Paul J. Ziemann. 2018. “Identification and Quantification of 4-Nitrocatechol Formed from OH and NO_3 Radical-Initiated Reactions of Catechol in Air in the Presence of NO_x: Implications for Secondary Organic Aerosol Formation from Biomass Burning.” *Environmental Science & Technology* 52 (4): 1981–89. https://doi.org/10.1021/acs.est.7b05864.

Forrister, Haviland, Jiumeng Liu, Eric Scheuer, Jack Dibb, Luke Ziemba, Kenneth L. Thornhill, Bruce Anderson, et al. 2015. “Evolution of Brown Carbon in Wildfire Plumes.” *Geophysical Research Letters* 42 (11): 4623–30. https://doi.org/10.1002/2015GL063897.

Foster, Katie, Rudra Pokhrel, Matthew Burkhart, and Shane Murphy. 2019. “A Novel Approach to Calibrating a Photoacoustic Absorption Spectrometer Using Polydisperse Absorbing Aerosol.” *Atmospheric Measurement Techniques* 12 (6): 3351–63. https://doi.org/10.5194/amt-12-3351-2019.

Garofalo, Lauren A., Matson A. Pothier, Ezra J. T. Levin, Teresa Campos, Sonia M. Kreidenweis, and Delphine K. Farmer. 2019. “Emission and Evolution of Submicron Organic Aerosol in Smoke from Wildfires in the Western United States.” *ACS Earth and Space Chemistry* 3 (7): 1237–47. https://doi.org/10.1021/acsearthspacechem.9b00125.

Garofalo, Lauren, Yicong He, Shantanu Jathar, Jeffrey Pierce, Carley Fredrickson, Joel Thornton, Brett Palm, et al. 2021. “Heterogeneous Nucleation Drives Particle Size Segregation in Sequential Ozone and Nitrate Oxidation of Catechol.” Submitted.

Gatzsche, Kathrin, Yoshiteru Iinuma, Andreas Tilgner, Anke Mutzel, Torsten Berndt, and Ralf Wolke. 2017. “Kinetic Modeling Studies of SOA Formation from α-Pinene Ozonolysis.” *Atmospheric Chemistry and Physics* 17 (21): 13187–211. https://doi.org/10.5194/acp-17-13187-2017.

Hallquist, M., J. C. Wenger, U. Baltensperger, Y. Rudich, D. Simpson, M. Claeys, J. Dommen, et al. 2009. “The Formation, Properties and Impact of Secondary Organic Aerosol:

Current and Emerging Issues." *Atmospheric Chemistry and Physics* 9 (14): 5155–5236. https://doi.org/10.5194/acp-9-5155-2009.

Hennigan, C. J., M. A. Miracolo, G. J. Engelhart, A. A. May, A. A. Presto, T. Lee, A. P. Sullivan, et al. 2011. "Chemical and Physical Transformations of Organic Aerosol from the Photo-Oxidation of Open Biomass Burning Emissions in an Environmental Chamber." *Atmospheric Chemistry and Physics* 11 (15): 7669–86. https://doi.org/10.5194/acp-11-7669-2011.

Huang, Wei, Harald Saathoff, Aki Pajunoja, Xiaoli Shen, Karl-Heinz Naumann, Robert Wagner, Annele Virtanen, Thomas Leisner, and Claudia Mohr. 2018. "α-Pinene Secondary Organic Aerosol at Low Temperature: Chemical Composition and Implications for Particle Viscosity." *Atmospheric Chemistry and Physics* 18 (4): 2883–98. https://doi.org/10.5194/acp-18-2883-2018.

Jaffe, Daniel A., and Nicole L. Wigder. 2012. "Ozone Production from Wildfires: A Critical Review." *Atmospheric Environment* 51 (May): 1–10. https://doi.org/10.1016/j.atmosenv.2011.11.063.

Joback, K.G., and R.C. Reid. 1987. "ESTIMATION OF PURE-COMPONENT PROPERTIES FROM GROUP-CONTRIBUTIONS." *Chemical Engineering Communications* 57 (1–6): 233–43. https://doi.org/10.1080/00986448708960487.

Jolly, W. Matt, Mark A. Cochrane, Patrick H. Freeborn, Zachary A. Holden, Timothy J. Brown, Grant J. Williamson, and David M. J. S. Bowman. 2015. "Climate-Induced Variations in Global Wildfire Danger from 1979 to 2013." *Nature Communications* 6 (1): 7537. https://doi.org/10.1038/ncomms8537.

Karanasiou, Angeliki, Andrés Alastuey, Fulvio Amato, Matteo Renzi, Massimo Stafoggia, Aurelio Tobias, Cristina Reche, et al. 2021. "Short-Term Health Effects from Outdoor Exposure to Biomass Burning Emissions: A Review." *Science of The Total Environment* 781 (August): 146739. https://doi.org/10.1016/j.scitotenv.2021.146739.

Koss, Abigail R., Kanako Sekimoto, Jessica B. Gilman, Vanessa Selimovic, Matthew M. Coggon, Kyle J. Zarzana, Bin Yuan, et al. 2018. "Non-Methane Organic Gas Emissions from Biomass Burning: Identification, Quantification, and Emission Factors from PTR-ToF during the FIREX 2016 Laboratory Experiment." *Atmospheric Chemistry and Physics* 18 (5): 3299–3319. https://doi.org/10.5194/acp-18-3299-2018.

Kovacic, Peter, and Ratnasamy Somanathan. 2014. "Nitroaromatic Compounds: Environmental Toxicity, Carcinogenicity, Mutagenicity, Therapy and Mechanism: Nitro Aromatic

Pollutants." *Journal of Applied Toxicology* 34 (8): 810–24. https://doi.org/10.1002/jat.2980.

Krechmer, Jordan E., Demetrios Pagonis, Paul J. Ziemann, and Jose L. Jimenez. 2016. "Quantification of Gas-Wall Partitioning in Teflon Environmental Chambers Using Rapid Bursts of Low-Volatility Oxidized Species Generated in Situ." *Environmental Science & Technology* 50 (11): 5757–65. https://doi.org/10.1021/acs.est.6b00606.

Kroflič, Ana, Miha Grilc, and Irena Grgić. 2015. "Does Toxicity of Aromatic Pollutants Increase under Remote Atmospheric Conditions?" *Scientific Reports* 5 (1): 8859. https://doi.org/10.1038/srep08859.

Lack, D. A., R. Bahreini, J. M. Langridge, J. B. Gilman, and A. M. Middlebrook. 2013. "Brown Carbon Absorption Linked to Organic Mass Tracers in Biomass Burning Particles." *Atmospheric Chemistry and Physics* 13 (5): 2415–22. https://doi.org/10.5194/acp-13-2415-2013.

Laskin, Alexander, Julia Laskin, and Sergey A. Nizkorodov. 2015. "Chemistry of Atmospheric Brown Carbon." *Chemical Reviews* 115 (10): 4335–82. https://doi.org/10.1021/cr5006167.

Lauraguais, Amélie, Cécile Coeur-Tourneur, Andy Cassez, Karine Deboudt, Marc Fourmentin, and Marie Choël. 2014. "Atmospheric Reactivity of Hydroxyl Radicals with Guaiacol (2-Methoxyphenol), a Biomass Burning Emitted Compound: Secondary Organic Aerosol Formation and Gas-Phase Oxidation Products." *Atmospheric Environment* 86 (April): 155–63. https://doi.org/10.1016/j.atmosenv.2013.11.074.

Lee, Ben H., Felipe D. Lopez-Hilfiker, Claudia Mohr, Theo Kurtén, Douglas R. Worsnop, and Joel A. Thornton. 2014. "An Iodide-Adduct High-Resolution Time-of-Flight Chemical-Ionization Mass Spectrometer: Application to Atmospheric Inorganic and Organic Compounds." *Environmental Science & Technology* 48 (11): 6309–17. https://doi.org/10.1021/es500362a.

Leuenberger, Christian, Jean Czuczwa, Josef Tremp, and Walter Giger. 1988. "Nitrated Phenols in Rain: Atmospheric Occurrence of Phytotoxic Pollutants." *Chemosphere* 17 (3): 511–15. https://doi.org/10.1016/0045-6535(88)90026-4.

Lin, Peng, Jiumeng Liu, John E. Shilling, Shawn M. Kathmann, Julia Laskin, and Alexander Laskin. 2015. "Molecular Characterization of Brown Carbon (BrC) Chromophores in Secondary Organic Aerosol Generated from Photo-Oxidation of Toluene." *Physical Chemistry Chemical Physics* 17 (36): 23312–25. https://doi.org/10.1039/C5CP02563J.

Lopez-Hilfiker, F. D., C. Mohr, M. Ehn, F. Rubach, E. Kleist, J. Wildt, Th. F. Mentel, et al. 2014. “A Novel Method for Online Analysis of Gas and Particle Composition: Description and Evaluation of a Filter Inlet for Gases and AEROsols (FIGAERO).” *Atmospheric Measurement Techniques* 7 (4): 983–1001. https://doi.org/10.5194/amt-7-983-2014.

———. 2015. “Phase Partitioning and Volatility of Secondary Organic Aerosol Components Formed from α-Pinene Ozonolysis and OH Oxidation: The Importance of Accretion Products and Other Low Volatility Compounds.” *Atmospheric Chemistry and Physics* 15 (14): 7765–76. https://doi.org/10.5194/acp-15-7765-2015.

Lopez-Hilfiker, F. D., C. Mohr, E. L. D’Ambro, A. Lutz, T. P. Riedel, C. J. Gaston, S. Iyer, et al. 2016. “Molecular Composition and Volatility of Organic Aerosol in the Southeastern U.S.: Implications for IEPOX Derived SOA.” *Environmental Science & Technology* 50 (5): 2200–09. https://doi.org/10.1021/acs.est.5b04769.

Mayorga, Raphael J., Zixu Zhao, and Haofei Zhang. 2021. “Formation of Secondary Organic Aerosol from Nitrate Radical Oxidation of Phenolic VOCs: Implications for Nitration Mechanisms and Brown Carbon Formation.” *Atmospheric Environment* 244 (January): 117910. https://doi.org/10.1016/j.atmosenv.2020.117910.

McDonald, Brian C., Joost A. de Gouw, Jessica B. Gilman, Shantanu H. Jathar, Ali Akherati, Christopher D. Cappa, Jose L. Jimenez, et al. 2018. “Volatile Chemical Products Emerging as Largest Petrochemical Source of Urban Organic Emissions.” *Science* 359 (6377): 760–64. https://doi.org/10.1126/science.aaq0524.

Millet, Dylan B., Munkhbayar Baasandorj, Lu Hu, Dhruv Mitroo, Jay Turner, and Brent J. Williams. 2016. “Nighttime Chemistry and Morning Isoprene Can Drive Urban Ozone Downwind of a Major Deciduous Forest.” *Environmental Science & Technology* 50 (8): 4335–42. https://doi.org/10.1021/acs.est.5b06367.

Mohr, Claudia, Felipe D. Lopez-Hilfiker, Peter Zotter, André S. H. Prévôt, Lu Xu, Nga L. Ng, Scott C. Herndon, et al. 2013. “Contribution of Nitrated Phenols to Wood Burning Brown Carbon Light Absorption in Detling, United Kingdom during Winter Time.” *Environmental Science & Technology* 47 (12): 6316–24. https://doi.org/10.1021/es400683v.

Myhre, G., D. Shindell, F.-M. Bréon, W. Collins, J. Fuglestvedt, J. Huang, D. Koch, J.-F. Lamarque, D. Lee, B. Mendoza, T. Nakajima, A. Robock, G. Stephens, T. Takemura and

H. Zhang, 2013: Anthropogenic and Natural Radiative Forcing. In: *Climate Change 2013: The Physical Science Basis. Contribution of Working Group I to the Fifth Assessment Report of the Intergovernmental Panel on Climate Change* [Stocker, T.F., D. Qin, G.-K. Plattner, M. Tignor, S.K. Allen, J. Boschung, A. Nauels, Y. Xia, V. Bex and P.M. Midgley (eds.)]. Cambridge University Press, Cambridge, United Kingdom and New York, NY, USA.

Myrdal, Paul B., and Samuel H. Yalkowsky. 1997. “Estimating Pure Component Vapor Pressures of Complex Organic Molecules.” *Industrial & Engineering Chemistry Research* 36 (6): 2494–99. https://doi.org/10.1021/ie950242l.

Nakao, S., C. Clark, P. Tang, K. Sato, and D. Cocker III. 2011. “Secondary Organic Aerosol Formation from Phenolic Compounds in the Absence of NO_x.” *Atmospheric Chemistry and Physics* 11 (20): 10649–60. https://doi.org/10.5194/acp-11-10649-2011.

Nannoolal, Yash, Jürgen Rarey, and Deresh Ramjugernath. 2008. “Estimation of Pure Component Properties.” *Fluid Phase Equilibria* 269 (1–2): 117–33. https://doi.org/10.1016/j.fluid.2008.04.020.

Nannoolal, Yash, Jürgen Rarey, Deresh Ramjugernath, and Wilfried Cordes. 2004. “Estimation of Pure Component Properties.” *Fluid Phase Equilibria* 226 (December): 45–63. https://doi.org/10.1016/j.fluid.2004.09.001.

Ng, N. L., S. C. Herndon, A. Trimborn, M. R. Canagaratna, P. L. Croteau, T. B. Onasch, D. Sueper, et al. 2011. “An Aerosol Chemical Speciation Monitor (ACSM) for Routine Monitoring of the Composition and Mass Concentrations of Ambient Aerosol.” *Aerosol Science and Technology* 45 (7): 780–94. https://doi.org/10.1080/02786826.2011.560211.

Palm, Brett B., Qiaoyun Peng, Carley D. Fredrickson, Ben H. Lee, Lauren A. Garofalo, Matson A. Pothier, Sonia M. Kreidenweis, et al. 2020. “Quantification of Organic Aerosol and Brown Carbon Evolution in Fresh Wildfire Plumes.” *Proceedings of the National Academy of Sciences* 117 (47): 29469–77. https://doi.org/10.1073/pnas.2012218117.

Pankow, J. F., and W. E. Asher. 2008. “SIMPOL.1: A Simple Group Contribution Method for Predicting Vapor Pressures and Enthalpies of Vaporization of Multifunctional Organic Compounds.” *Atmospheric Chemistry and Physics* 8 (10): 2773–96. https://doi.org/10.5194/acp-8-2773-2008.

Pereira, Kelly L., Jacqueline F. Hamilton, Andrew R. Rickard, William J. Bloss, Mohammed S. Alam, Marie Camredon, Martyn W. Ward, et al. 2015. “Insights into the Formation and Evolution of Individual Compounds in the Particulate Phase during Aromatic Photo-

Oxidation.” *Environmental Science & Technology* 49 (22): 13168–78. https://doi.org/10.1021/acs.est.5b03377.

Pye, Havala O. T., Andreas Zuend, Juliane L. Fry, Gabriel Isaacman-VanWertz, Shannon L. Capps, K. Wyat Appel, Hosein Foroutan, Lu Xu, Nga L. Ng, and Allen H. Goldstein. 2018. “Coupling of Organic and Inorganic Aerosol Systems and the Effect on Gas–Particle Partitioning in the Southeastern US.” *Atmospheric Chemistry and Physics* 18 (1): 357–70. https://doi.org/10.5194/acp-18-357-2018.

Romonosky, Dian E., Alexander Laskin, Julia Laskin, and Sergey A. Nizkorodov. 2015. “High-Resolution Mass Spectrometry and Molecular Characterization of Aqueous Photochemistry Products of Common Types of Secondary Organic Aerosols.” *The Journal of Physical Chemistry A* 119 (11): 2594–2606. https://doi.org/10.1021/jp509476r.

Ruggeri, Giulia, Fabian A. Bernhard, Barron H. Henderson, and Satoshi Takahama. 2016. “Model–Measurement Comparison of Functional Group Abundance in α-Pinene and 1,3,5-Trimethylbenzene Secondary Organic Aerosol Formation.” *Atmospheric Chemistry and Physics* 16 (14): 8729–47. https://doi.org/10.5194/acp-16-8729-2016.

Saleh, Rawad, Ellis S. Robinson, Daniel S. Tkacik, Adam T. Ahern, Shang Liu, Allison C. Aiken, Ryan C. Sullivan, et al. 2014. “Brownness of Organics in Aerosols from Biomass Burning Linked to Their Black Carbon Content.” *Nature Geoscience* 7 (9): 647–50. https://doi.org/10.1038/ngeo2220.

Schobesberger, Siegfried, Emma L. D’Ambro, Felipe D. Lopez-Hilfiker, Claudia Mohr, and Joel A. Thornton. 2018. “A Model Framework to Retrieve Thermodynamic and Kinetic Properties of Organic Aerosol from Composition-Resolved Thermal Desorption Measurements.” *Atmospheric Chemistry and Physics* 18 (20): 14757–85. https://doi.org/10.5194/acp-18-14757-2018.

Short, Karen C. 2015. “Sources and Implications of Bias and Uncertainty in a Century of US Wildfire Activity Data.” *International Journal of Wildland Fire* 24 (7): 883. https://doi.org/10.1071/WF14190.

Song, Chen, Rahul A. Zaveri, John E. Shilling, M. Lizabeth Alexander, and Matt Newburn. 2011. “Effect of Hydrophilic Organic Seed Aerosols on Secondary Organic Aerosol Formation from Ozonolysis of α-Pinene.” *Environmental Science & Technology* 45 (17): 7323–29. https://doi.org/10.1021/es201225c.

Stark, Harald, Reddy L. N. Yatavelli, Samantha L. Thompson, Hyungu Kang, Jordan E. Krechmer, Joel R. Kimmel, Brett B. Palm, et al. 2017. “Impact of Thermal Decomposition on Thermal Desorption Instruments: Advantage of Thermogram Analysis for Quantifying Volatility Distributions of Organic Species.” *Environmental Science & Technology* 51 (15): 8491–8500. https://doi.org/10.1021/acs.est.7b00160.

Stein, S. E., and R. L. Brown. 1994. “Estimation of Normal Boiling Points from Group Contributions.” *Journal of Chemical Information and Computer Sciences* 34 (3): 581–87. https://doi.org/10.1021/ci00019a016.

Sullivan, A. P., H. Guo, J. C. Schroder, P. Campuzano-Jost, J. L. Jimenez, T. Campos, V. Shah, et al. 2019. “Biomass Burning Markers and Residential Burning in the WINTER Aircraft Campaign.” *Journal of Geophysical Research: Atmospheres* 124 (3): 1846–61. https://doi.org/10.1029/2017JD028153.

Thornton, Joel A., Claudia Mohr, Siegfried Schobesberger, Emma L. D’Ambro, Ben H. Lee, and Felipe D. Lopez-Hilfiker. 2020. “Evaluating Organic Aerosol Sources and Evolution with a Combined Molecular Composition and Volatility Framework Using the Filter Inlet for Gases and Aerosols (FIGAERO).” *Accounts of Chemical Research* 53 (8): 1415–26. https://doi.org/10.1021/acs.accounts.0c00259.

Traversi, Deborah, Raffaella Degan, Roberto De Marco, Giorgio Gilli, Cristina Pignata, Simona Villani, and Roberto Bono. 2009. “Mutagenic Properties of PM2.5 Urban Pollution in the Northern Italy: The Nitro-Compounds Contribution.” *Environment International* 35 (6): 905–10. https://doi.org/10.1016/j.envint.2009.03.010.

Yee, L. D., K. E. Kautzman, C. L. Loza, K. A. Schilling, M. M. Coggon, P. S. Chhabra, M. N. Chan, et al. 2013. “Secondary Organic Aerosol Formation from Biomass Burning Intermediates: Phenol and Methoxyphenols.” *Atmospheric Chemistry and Physics* 13 (16): 8019–43. https://doi.org/10.5194/acp-13-8019-2013.

Ylisirniö, Arttu, Luis M. F. Barreira, Iida Pullinen, Angela Buchholz, John Jayne, Jordan E. Krechmer, Douglas R. Worsnop, Annele Virtanen, and Siegfried Schobesberger. 2021. “On the Calibration of FIGAERO-ToF-CIMS: Importance and Impact of Calibrant Delivery for the Particle-Phase Calibration.” *Atmospheric Measurement Techniques* 14 (1): 355–67. https://doi.org/10.5194/amt-14-355-2021.

Appendix A. TOTAL EXPERIMENTAL CHAMBER CONDITIONS

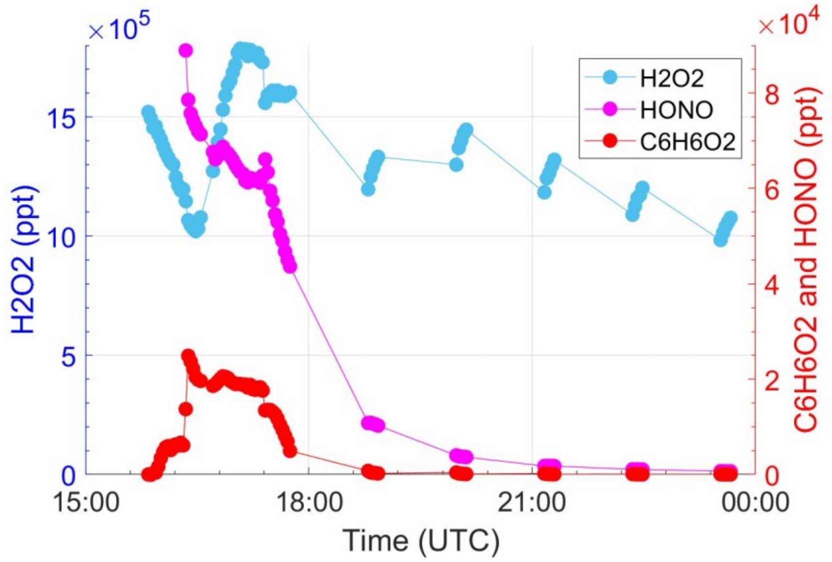

Figure A1. Gas-phase concentrations of injected oxidants and catechol ($C_6H_6O_2$) for the 06/03 catechol + OH/NO_x experiment.

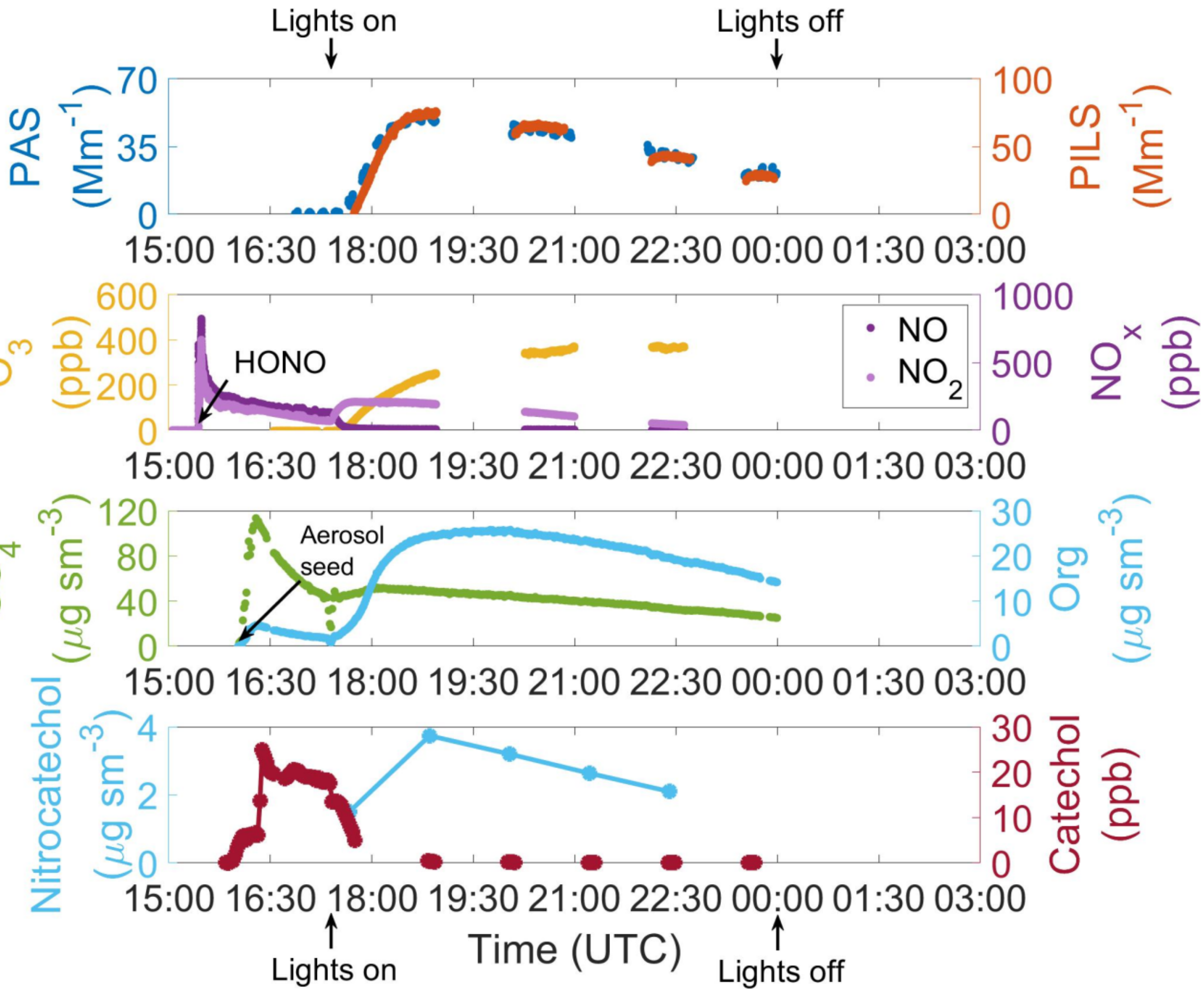

Figure A2. Absorption at 405 nm as measured by the PAS and PILS-LWCC-TOC; O_3, NO, and NO_2; AMS SO_4 and AMS OA; and particle-phase nitrocatechol and gas-phase catechol are plotted across four windows for the 06/03 catechol + OH/NO_x experiment. Chamber events are labeled with arrows and descriptive text.

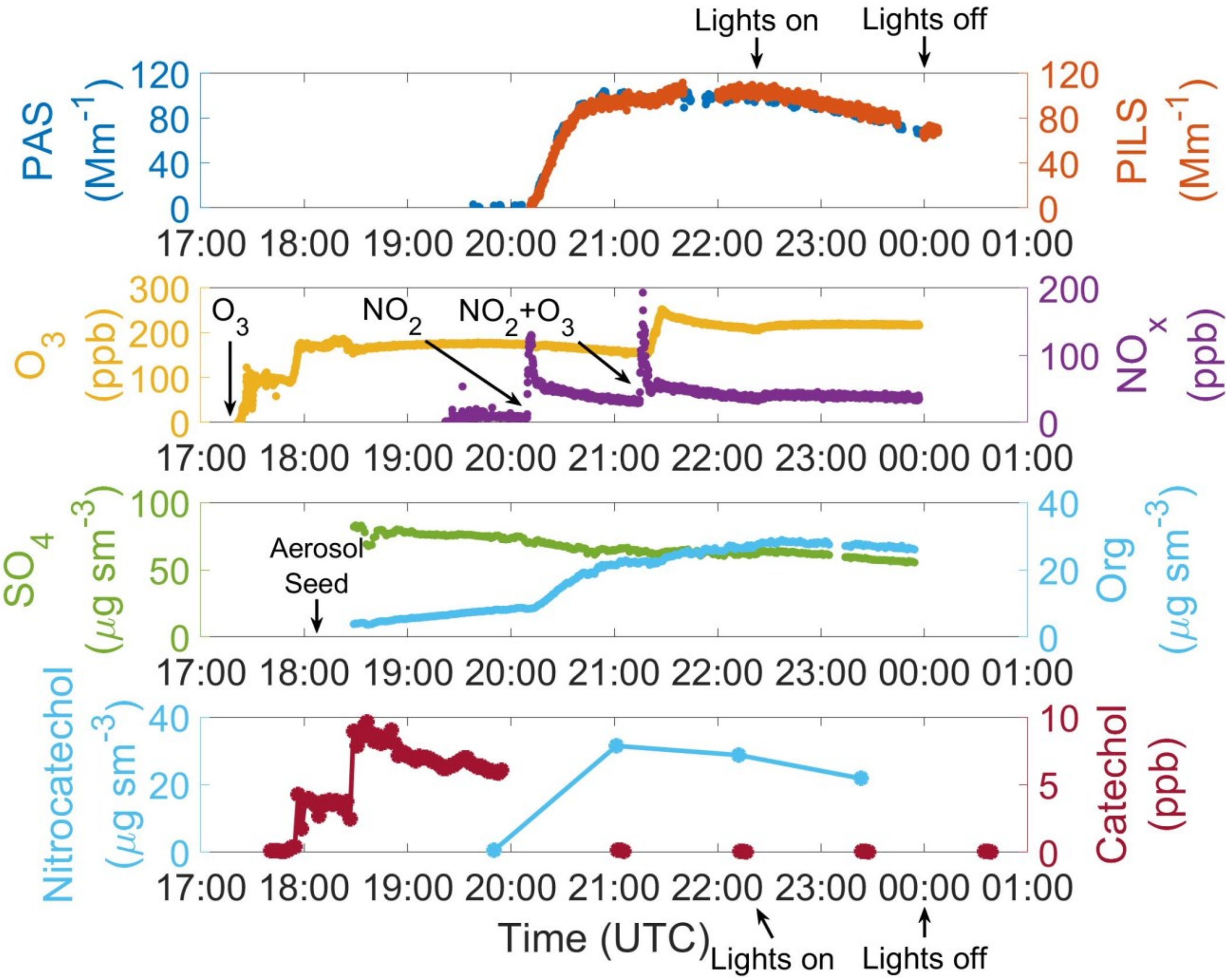

Figure A3. Same as Figure A2 but for the 06/04 catechol + O_3 + NO_3 experiment.

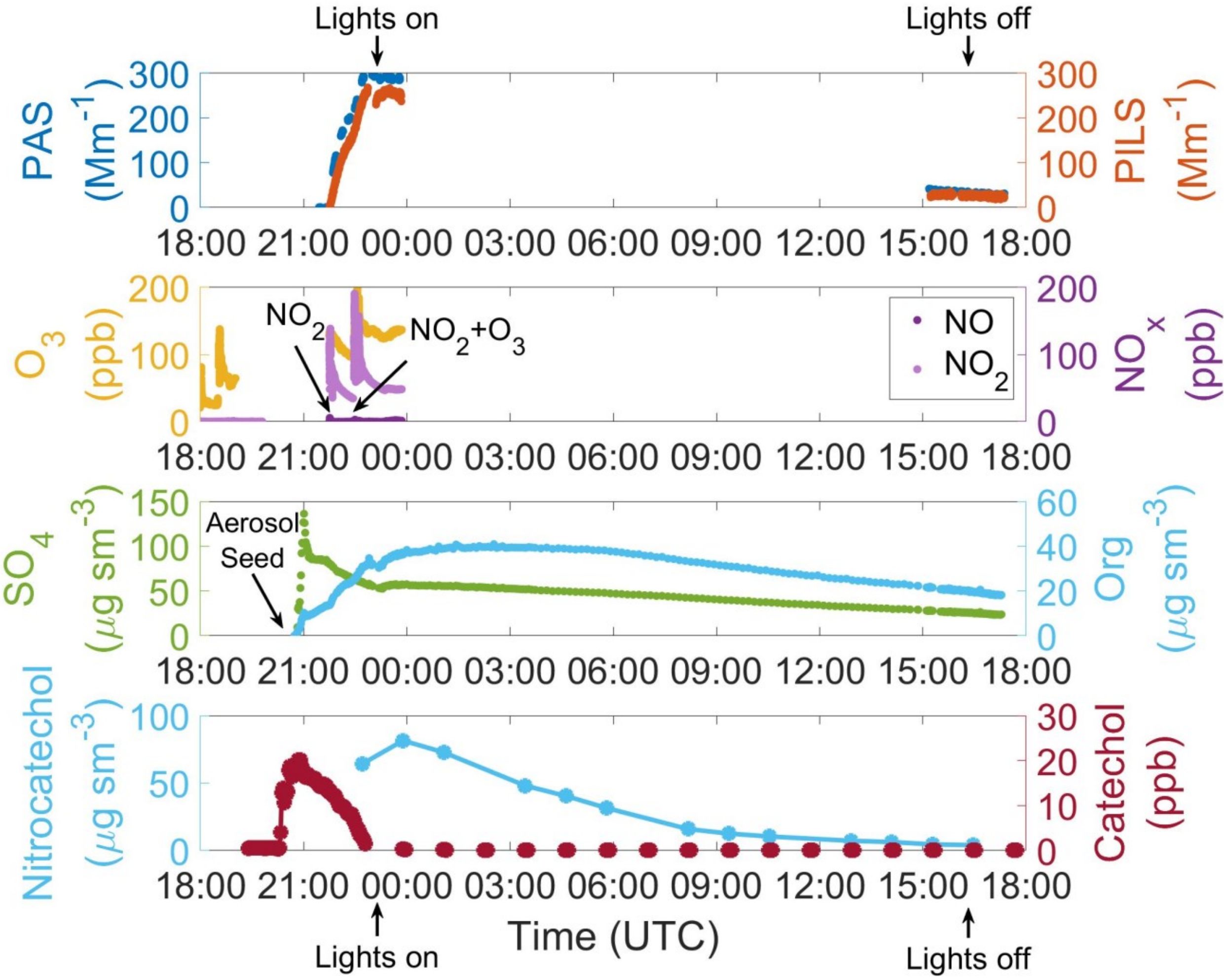

Figure A4. Same as Figure A2 but for the 06/05 catechol + O_3 + NO_3 extended experiment.

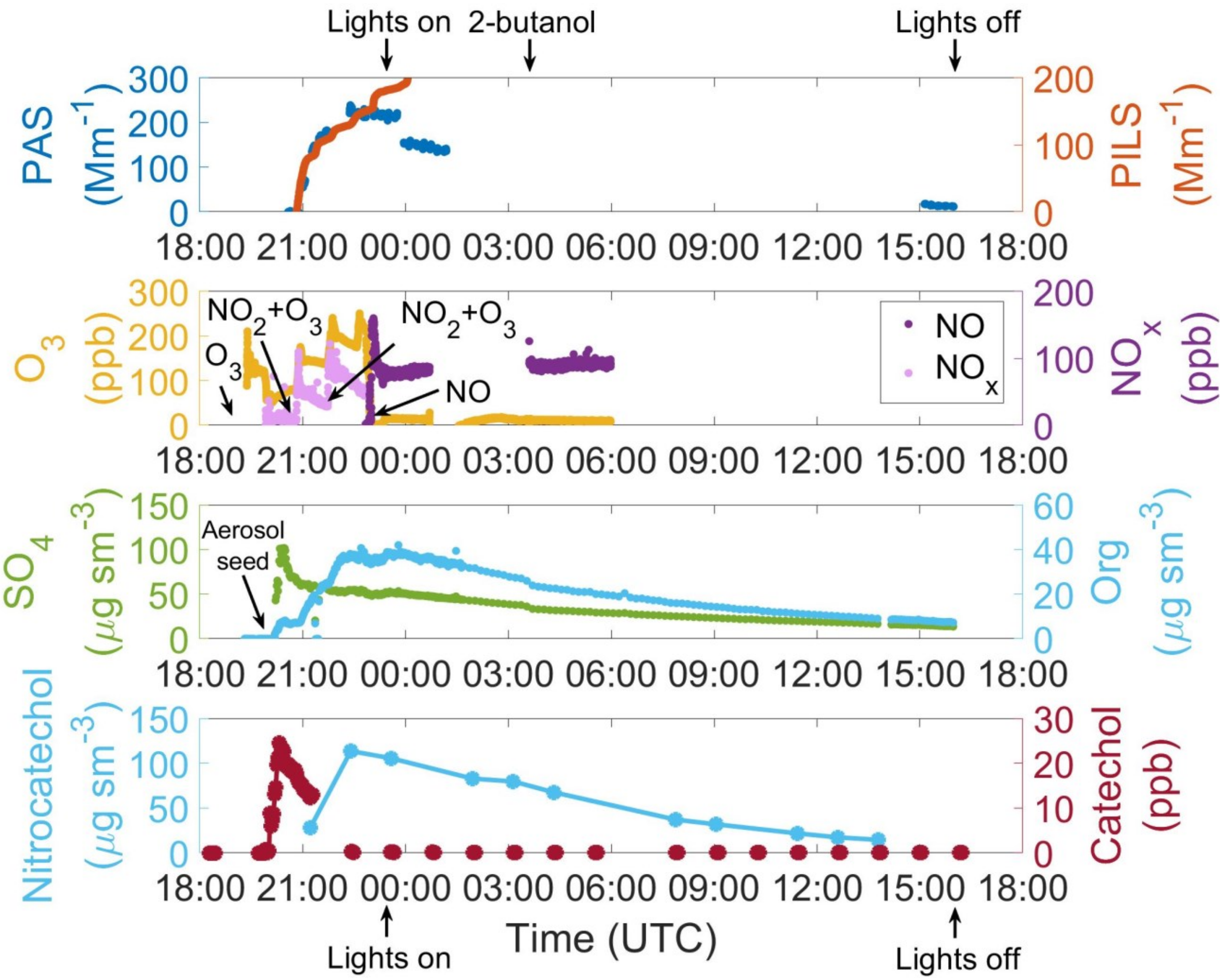

Figure A5. Same as Figure A2 but for the 06/14 catechol + O_3 + NO_3 extended experiment.

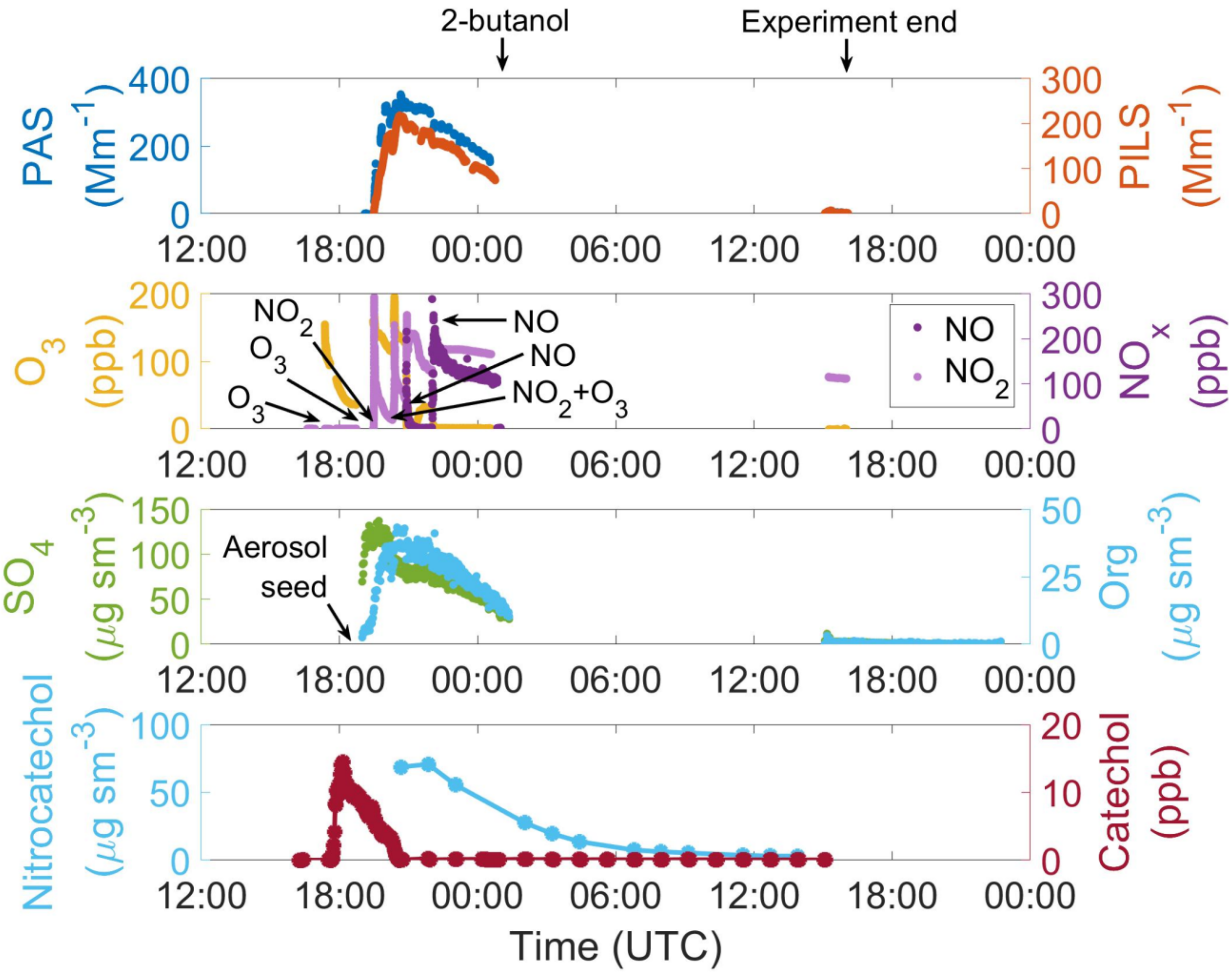

Figure A6. Same as Figure A2 but for the 06/22 catechol + O_3 + NO_3 dark extended experiment.

Appendix B. EVERY EXPERIMENT NITROCATECHOL THERMOGRAMS

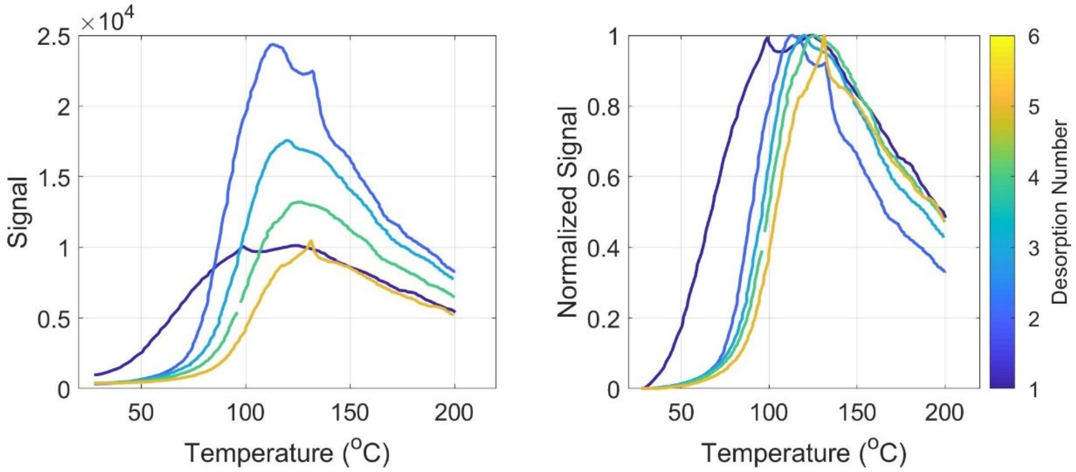

Figure B1. Same as **Figure 4**, but for the 06/03 catechol + OH/NO$_x$ experiment. Note that the first desorption (dark blue trace) had a different temperature ramp rate, so comparisons should not be made. T$_{max}$ increased with each desorption, but the average is 119.4 °C or $C^* = 1.3 \times 10^{-5}$ µg m^{-3}.

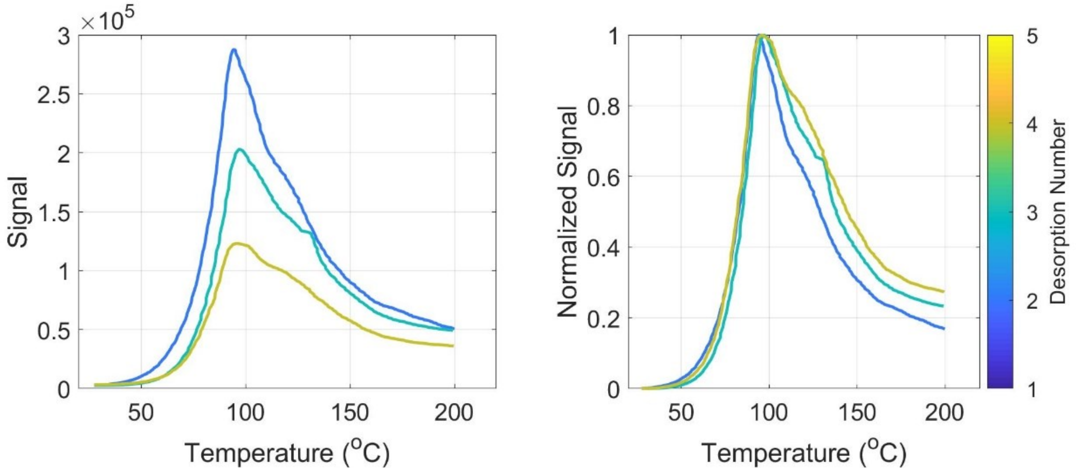

Figure B2. Same as **Figure 4**, but for the 06/04 catechol + O$_3$ + NO$_3$ experiment. Average T$_{max}$ is 95.9 °C or $C^* = 2.7 \times 10^{-3}$ µg m^{-3}.

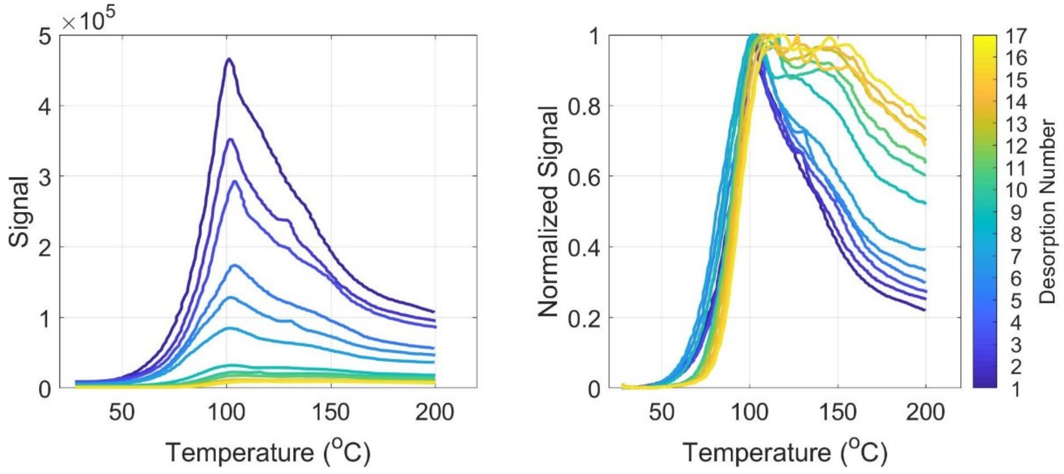

Figure B3. Same as **Figure 4**, but for the 06/05 catechol + O_3 + NO_3 extended experiment. Average T_{max} is 102.5 °C or $C^* = 6.0 \times 10^{-4}$ µg m^{-3}.

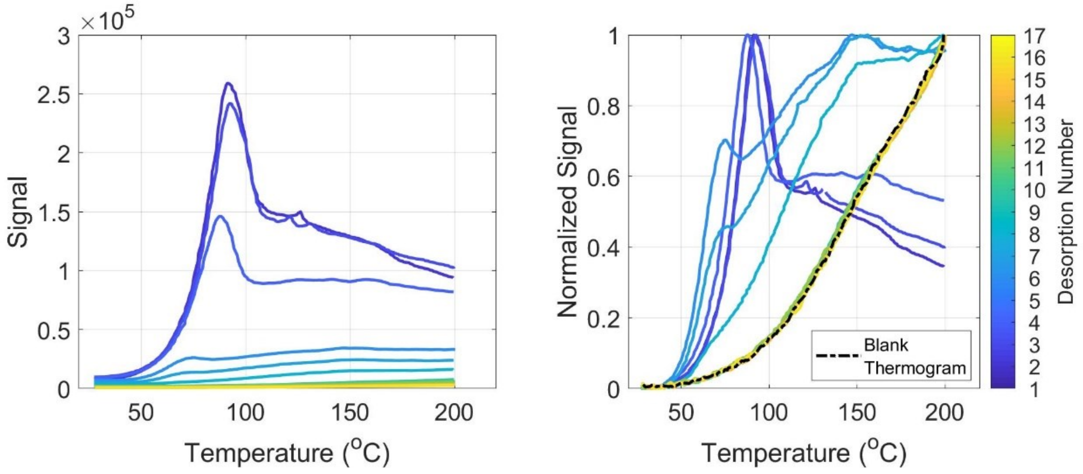

Figure B4. Same as **Figure 4**, but for the 06/22 catechol + O_3 + NO_3 dark extended experiment. Average T_{max} is 91.0 °C or $C^* = 8.2 \times 10^{-3}$ µg m^{-3}.

Appendix C. ADDITIONAL CATECHOL EXPERIMENT ABSORPTION DECAY

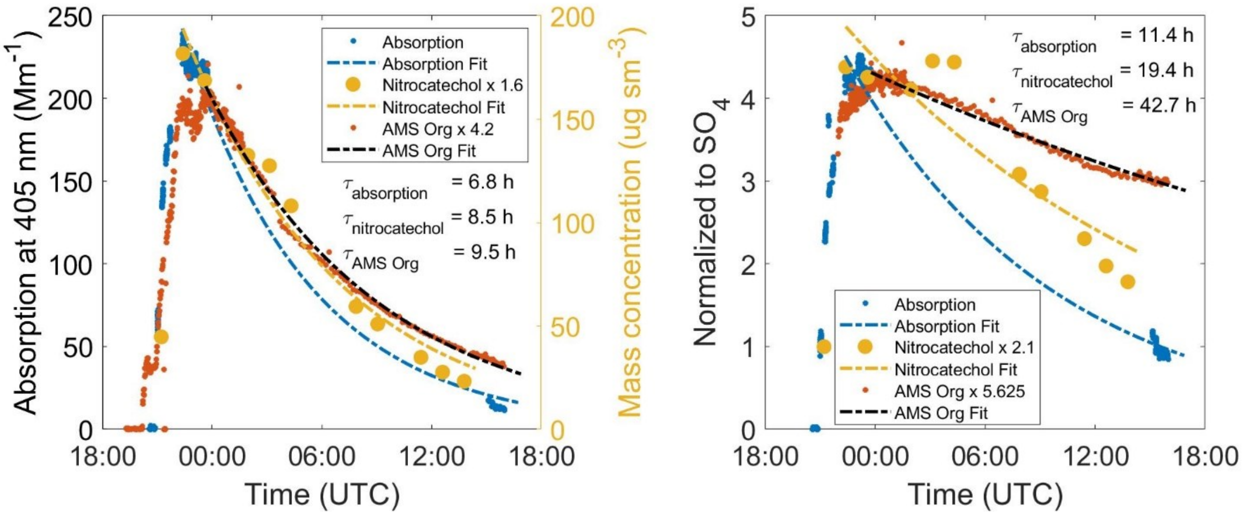

Figure C1. Same as **Figure 9** in main text, but for the 06/14 catechol + O_3 + NO_3 extended experiment.

Appendix D. FIGAERO-CIMS OA AND AMS OA TRENDS

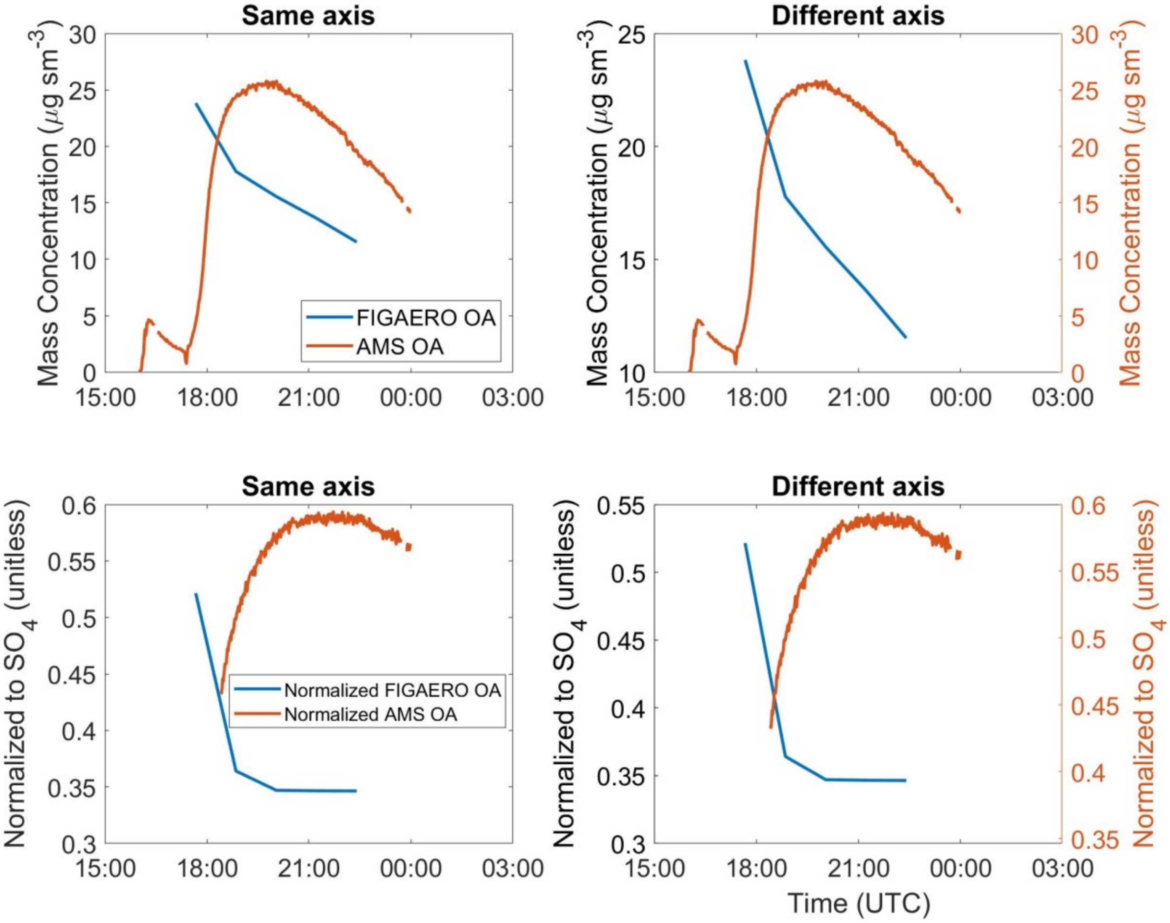

Figure D1. For the 06/03 catechol + OH/NO$_x$ experiment, (a) in the upper left, the time series of the AMS OA and FIGAERO-CIMS OA mass concentrations is plotted on the same axis, (b) in the upper right, it is the same as (a) but with each variable plotted on different axes, (c) in the lower left, it is the same as (a) but with both variables normalized to AMS SO$_4$, and (d) in the lower right, it is the same as (b) but with both variables normalized to AMS SO$_4$.

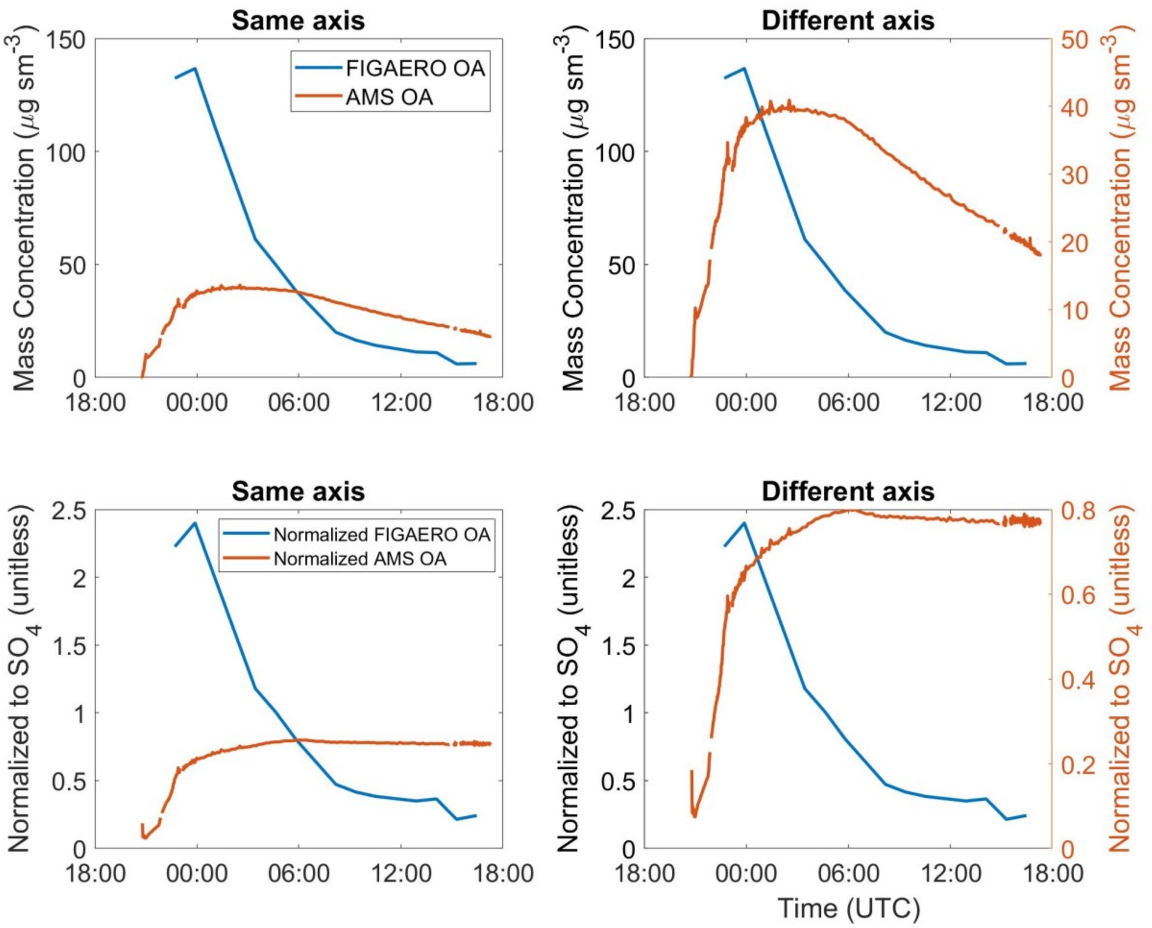

Figure D2. Same as Figure D1, but for the 06/05 catechol + O_3 + NO_3 extended experiment.

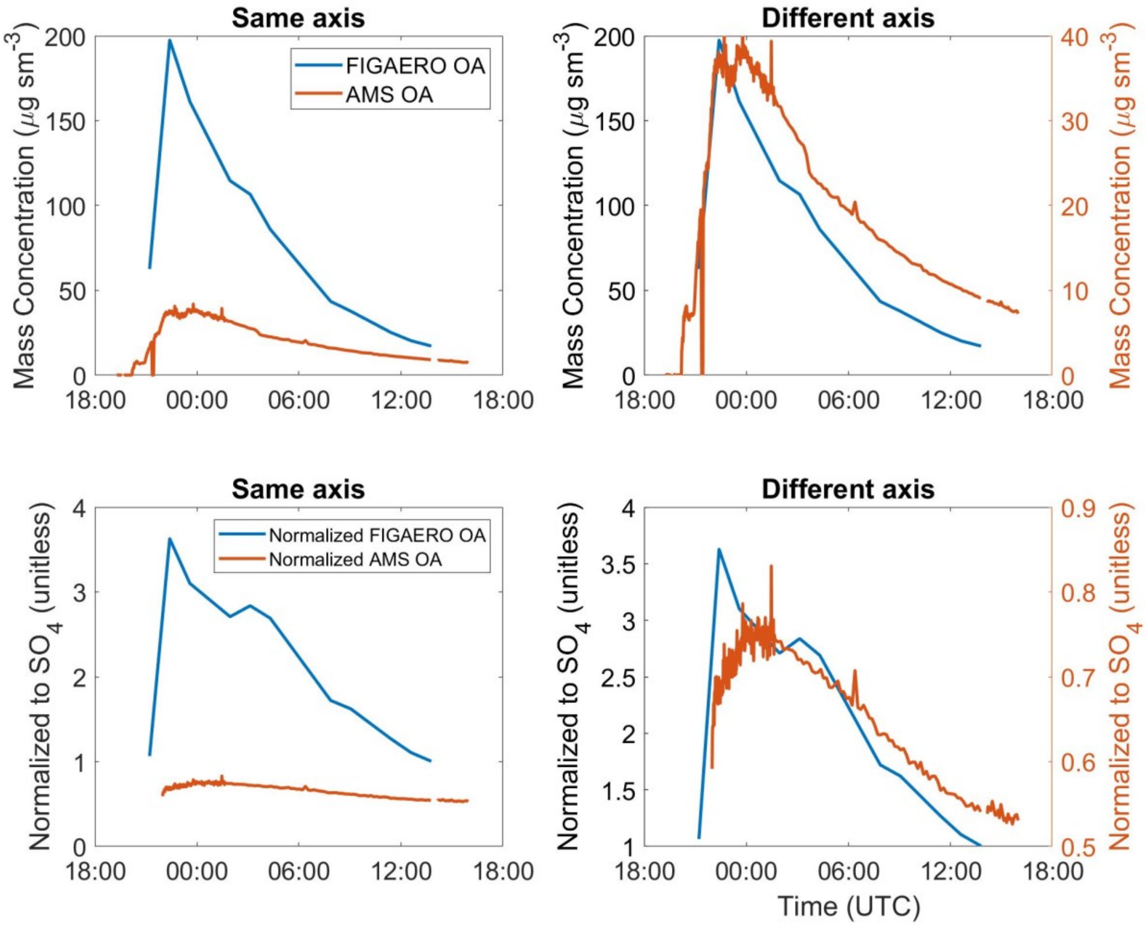

Figure D3. Same as Figure D1, but for the 06/14 catechol + O_3 + NO_3 extended experiment.

Appendix E. NITROCATECHOL DIVIDED THERMOGRAM CONTRIBUTIONS

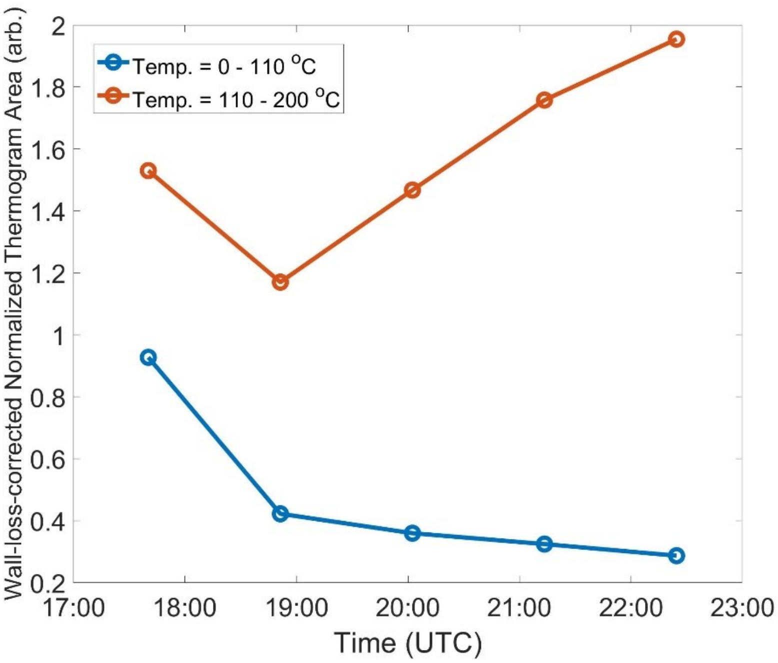

Figure E1. Same as **Figure 5**, but for the 06/03 catechol + OH/NO_x experiment.

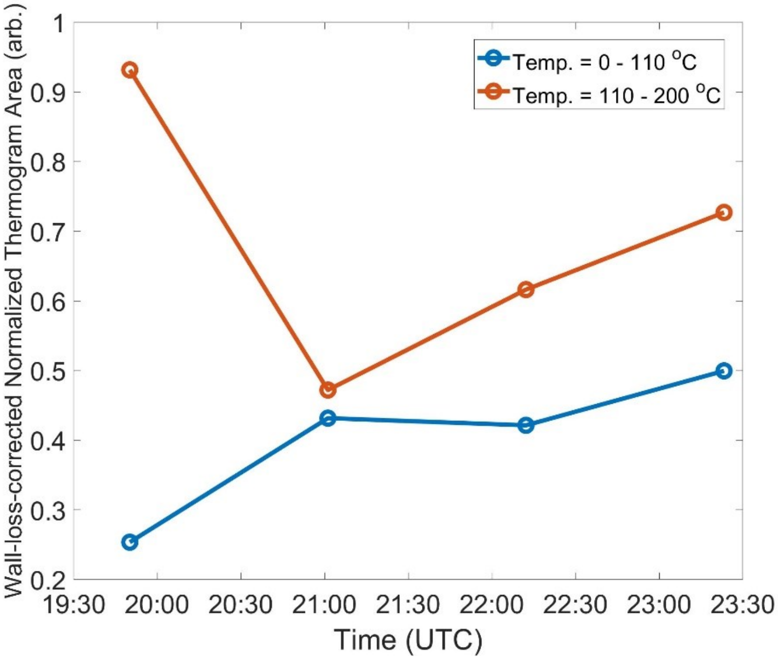

Figure E2. Same as **Figure 5**, but for the 06/04 catechol + O_3 + NO_3 experiment.

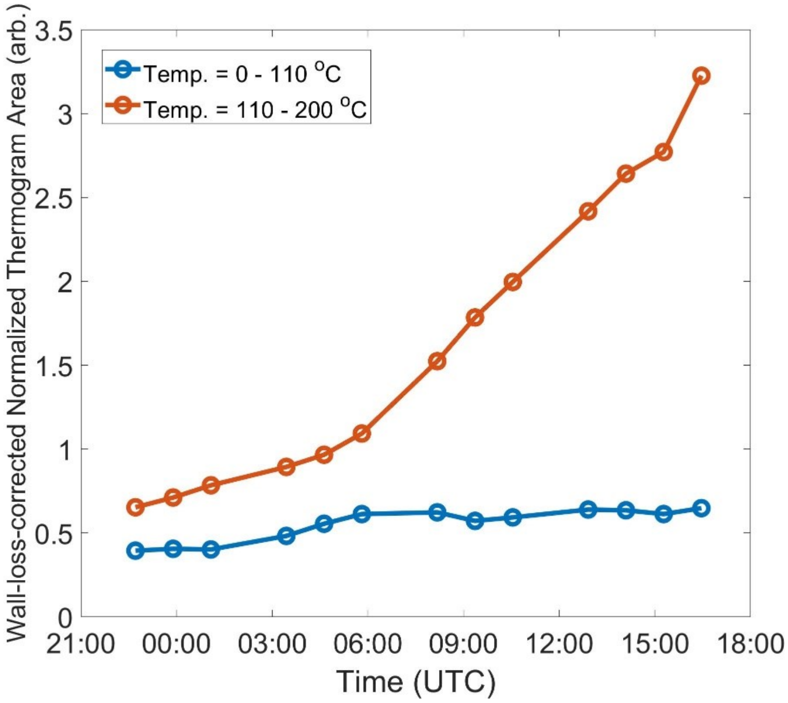

Figure E3. Same as **Figure 5**, but for the 06/05 catechol + O_3 + NO_3 extended experiment.

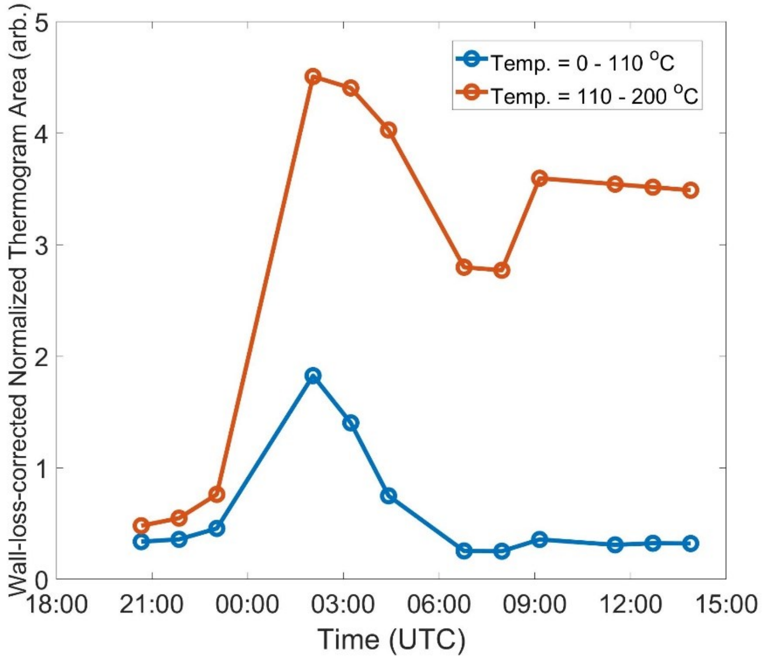

Figure E4. Same as **Figure 5**, but for the 06/22 catechol + O_3 + NO_3 dark extended experiment.

VITA

Carley Fredrickson is an Atmospheric Sciences graduate student and Achievement Rewards for College Scientists (ARCS) Fellow in Dr. Joel Thornton’s group at the University of Washington. Prior to joining Dr. Joel Thornton’s group, she interned at the Brookhaven National Laboratory where she conducted air quality research and measurements on black carbon emitted from wood-burning boilers. She graduated with highest honors from the University of California, Davis in 2017, where she was an Atmospheric Science major, Mathematics minor, and focused on atmospheric chemistry, air quality modeling, and aerosol remote observations in her coursework and research.